

REMARKS/ ARGUMENTS

The Office Action of August 11, 2004 has been carefully reviewed and this response addresses the Examiner's concerns.

Support for the Amendments to the Specification

The amendments to the specification do not introduce new matter. The amendments to the specification follow the Examiner's request and address typographical errors.

Support for Amendments to the Drawings

A Replacement Sheet for Figure 2 is attached. The amendment to the Figure 2 does not introduce new matter. In referring to Fig. 2 in the specification, lines 17-18 of paragraph [0025] refer to "Applying a signal to driver 75." Driver 75 was missing from Fig. 2. In paragraph [0023] and in Fig. 1, a driver 60 for another switchable pixellated element is shown. The Replacement Sheet for Figure 2 includes a driver 75 for the pixellated switchable optical element 70.

Status of the Claims

Claims 1-21 were pending in the application.

Claims 1, 8-11, 13-15 and 21 are amended in order to more clearly express the invention.

Claim 2 is canceled without prejudice.

Claim 13 was rejected under 35 USC 112, first paragraph as being indefinite. Claims 8-17 were rejected under 35 USC 112, second paragraph, as being incomplete.

Claims 1-13, 18 and 21 were rejected under 35 U.S.C. §102(e) as being anticipated by Bouevitch (U.S. Patent Publication No. US2003/0021526). Claims 14-17 and 19-20 were rejected under 35 U.S.C. §103(a) as being unpatentable over Bouevitch (U.S. Patent Publication No. US2003/0021526) in view of Shirasaki et al. (U.S. Patent Publication No. US2002/0114090).

The 35 U.S.C. §112 rejection

Claim 13 was rejected under 35 USC 112, first paragraph as being indefinite. Claims 8-17 were rejected under 35 USC 112, second paragraph, as being incomplete.

The amended claims 13, 8, and 14, rewritten in order to more clearly express the invention, overcome the 35 USC 112 rejections.

Claim 8 is amended, adding the following statement:

"said volume holographic mirror being optically disposed between said optical separating sub-system and said optical recombining sub-system." The statement provides a cooperative relationship between the elements.

Claim 14 is amended by presenting the recombining diffraction gratings after the switchable element and describing the recombining diffraction gratings as:

"a pair of recombining diffraction gratings capable of recombining said outputted separated distinct chromatic components", where the switchable element is capable of receiving the separated distinct chromatic components and outputting separated distinct output chromatic components. The statement provides a cooperative relationship between the elements.

The 35 U.S.C. §102 rejection

Claims 1-13, 18 and 21 were rejected under 35 U.S.C. §102(e) as being anticipated by Bouevitch (U.S. Patent Publication No. US2003/0021526).

Applicants respectfully request the Examiner reconsider the rejection of claims 1-13, 18 and 21 based upon the amendments set forth above and the remarks set forth herein and below.

To anticipate a claim a reference must teach every element of the claim. (MPEP § 2131). "A claim is anticipated only if each and every element as set forth in the claim is found, either expressly or inherently described, in a single prior art reference." *Verdegaal Bros. v. Union Oil Co. of California*, 814 F.2d 628, 631, 2 USPQ2d 1051, 1053 (Fed. Cir. 1987).

The first step in determining whether a claim is anticipated is to interpret the claim. ("It is elementary in patent law that, in determining whether a patent is valid the first step

is to determine the meaning and scope of each claim in suit." *Lemelson v. Gen. Mills, Inc.*, 968 F.2d 1202, 1206, 23 U.S.P.Q.2D (BNA) 1284, 1287 (Fed. Cir. 1992).) When not defined by applicant in the specification, the words of a claim must be read as they would be interpreted by those of ordinary skill in the art. (MPEP 211.01) (*Rexnord Corp. v. Laitram Corp.*, 274 F.3d 1336, 1342, 60 USPQ2d 1851, 1854 (Fed. Cir. 2001) ("explaining the court's analytical process for determining the meaning of disputed claim terms").

Amended independent claim 1 claims a step of "reflecting said distinct chromatic components from a holographic mirror," and amended independent claims 8 and 14 claim, respectively, a volume holographic mirror and a holographic mirror as elements.

A holographic mirror to one of ordinary skill in the art refers to a reflection type hologram where the reflection is accomplished by diffraction of the incident radiation. (See, for example, J. R. Magariños, D. J. Coleman, *Holographic Mirrors*, Optical Engineering, Vol. 24(5), p. 770, 1985, a copy of which is enclosed in the Appendix. See also, for example, papers reprinted in *Selected Papers in Holographic and Diffractive Lenses and Mirrors*, edited by Thomas W. Stone and Brian J. Thompson, ISBN 0-8194-0637-6). A hologram to one of ordinary skill in the art refers to an "interference pattern that is recorded on a high-resolution medium [plate], the two interfering beams formed by a coherent beam from a laser and light scattered by an object" (see, for example, <http://www.photonics.com/dictionary/lookup/XQ/ASP/url.lookup/entrynum.2397/letter.h/pu./QX/lookup.htm>).

The Examiner asserts that Bouevitch discloses a switchable holographic mirror in paragraph [0086], lines 4-5 and Fig. 5b. Applicant respectfully asserts for the reasons given below that Bouevitch does not disclose a holographic mirror, whether switchable or not switchable.

In paragraph [0086], lines 1-6, Bouevitch (U.S. Patent Publication No. US2003/0021526) states that:

FIG. 5b illustrates an alternative arrangement for a tunable etalon 550 in which the front partially reflective surface 525 is in the form of a dielectric coating on a substrate 551, and the rear fully reflective

coating is in the form of an array of piston MEMS mirrors 552 formed in a substrate 553.

A MEMS mirror is a micro-electromechanical mirror system.

Bouevitch does not disclose an interference pattern that is recorded on a high-resolution medium. Bouevitch also does not disclose an element in which the reflection is accomplished by diffraction of the incident radiation.

In the element disclosed by Bouevitch in paragraph [0086], lines 1-6, reflection occurs by a front partially reflective surface 525 in the form of a dielectric coating on a substrate 551 and by a rear fully reflective coating in the form of an array of piston MEMS mirrors. The reflection from a dielectric coating is a consequence of the boundary conditions for the electromagnetic fields at an interface, which is the usual reflection mechanism (see, for example, E. Hetch, *Optics*, ISBN 0-201-11609-X, pp. 92-102, a copy of which is enclosed in the Appendix). A MEMS mirror is a traditional mirror (see, for example, Lau, K.Y., *MEM's the word for optical beam manipulation*, IEEE Circuits and Devices Magazine, Vol. 13, No. 4, July 1997, pp.11-18, a copy of which is enclosed in the Appendix). Thus, the element disclosed by Bouevitch is a mirror with a dielectric coating and the reflection is a consequence of the boundary conditions for the electromagnetic fields at the interfaces, which is the usual reflection mechanism.

Therefore, the element disclosed by Bouevitch does not include an interference pattern that is recorded on a high-resolution medium and is not an element in which the reflection is accomplished by diffraction of the incident radiation. Therefore, Applicant respectfully states that Bouevitch does not disclose a holographic mirror. Applicant also respectfully states that Bouevitch does not disclose "reflecting said distinct chromatic components from a holographic mirror," or a volume holographic mirror. Due to the difference in operation of the holographic mirror as compared to the simple reflector disclosed by Bouevitch, there are intrinsic characteristics and advantages of the Applicant's invention which are absent in Bouevitch.

To anticipate a claim a reference must teach every element of the claim. (MPEP § 2131).

As pointed above, Bouevitch does not teach "reflecting said distinct chromatic components from a holographic mirror," a system including a volume holographic mirror, or a system including a holographic mirror.

Applicant respectfully asserts that amended independent Claims 1, 8 are not anticipated by Bouevitch and neither are any of the dependent claims. In addition, in view of the specific needs of Bouevitch (as discussed above) and since Bouevitch is lacking at least one patentable feature present in Claims 1, 8, and the dependent claims of the Applicants' invention, a modification of Bouevitch under 35 U.S.C. §103 would also be inapplicable because such modifications are not taught by nor obvious under Bouevitch, and if incorporated into Bouevitch, would render Bouevitch unsuitable for its intended functions.

The 35 U.S.C. §103 rejection

Claims 14-17 and 19-20 were rejected under 35 U.S.C. §103(a) as being unpatentable over Bouevitch (U.S. Patent Publication No. US2003/0021526) in view of Shirasaki et al. (U.S. Patent Publication No. US2002/0114090).

As stated above, Bouevitch does not disclose a volume holographic mirror, or a holographic mirror. Shirasaki et al. do not disclose a volume holographic mirror, or a holographic mirror. Therefore combining Bouevitch. with Shirasaki et al. cannot be used to establish nor disclose a volume holographic mirror, or a holographic mirror.

Under a 103 rejection, a *prima facie* case of obviousness of the invention is made in view of the scope and content of the prior art. In order to establish a *prima facie* case of obviousness, "there must be some suggestion or motivation, either in the references themselves or in the knowledge generally available to one of ordinary skill in the art, to modify the reference or to combine reference teachings. Second, there must be a reasonable expectation of success. Finally, the prior art reference (or references) must teach or suggest all of the claim limitations." MPEP § 2143.

Neither Bouevitch nor Shirasaki et al. separately or in combination teach all the patentable features of amended claims 8 or 14 and the dependent claims, such as claims 15-17, and 19-20. In light thereof, Applicant respectfully traverses the 35 U.S.C. 103 rejection of the claims.

In conclusion, in view of the above remarks, Applicant respectfully requests the Examiner find claims, 1, 2- 21 as amended, allowable over the prior art and pass this case to issue.

Since the total number of claims is less than the number of claims already been paid for, no additional fees are required. However, if fees are required, they should be charged to Deposit Account No. 50-1078.

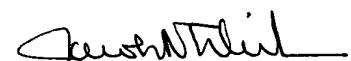
In accordance with Section 714.01 of the MPEP, the following information is presented in the event that a call may be deemed desirable by the Examiner:

JACOB N. ERLICH (617) 854-4000

Respectfully submitted,
Thomas W. Stone, Applicant

Dated: November 10, 2004

By:


Jacob N. Erlich
Reg. No. 24,338
Attorney for Applicant



MEM'S THE WORD FOR OPTICAL BEAM MANIPULATION

Building Microelectromechanical-Based Optical Systems on a Silicon Chip

Most optical systems require precise alignment of optical components, as well as switching, scanning, or other manipulations of optical beams. These functions are required when the system is being assembled and possibly on a continuous basis thereafter during operation. An entire industry has grown up that manufactures precise, bulk-mechanical devices that enable such tasks to be performed with comparative ease. Even though they are indispensable as laboratory tools, these mechanical devices have acquired the stigma of being costly and unreliable in field use.

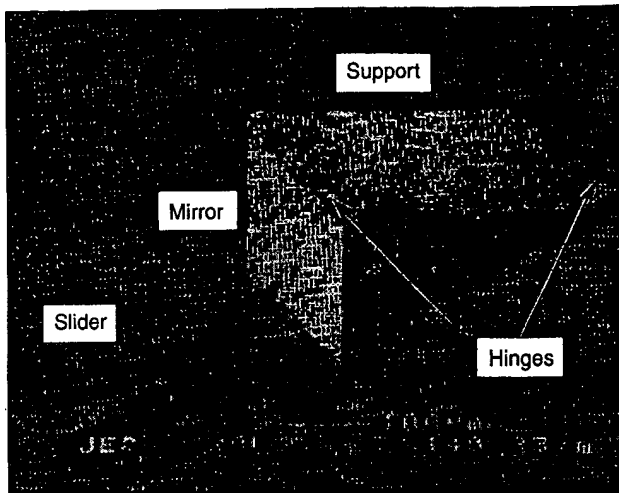
The vision to build optical systems with "nonmoving parts" has inspired three decades of research in optical interactions in linear and nonlinear materials, with the goal of manipulating an optical beam by electro-magnetic and acoustic fields or even by other optical beams. The electro-optic and magneto-optic effects or other higher-order nonlinear effects exploited for this purpose are very small in most materials, and beam deflection using acousto-optic effect is far from being 100% efficient. These effects have found applications in various niche situations but are far from being able to replace micropositioners and other mundane mechanical devices in constructing a fully functional optical system.

One has to face the fact that perhaps the best way to switch the direction of an optical beam is simply to rotate a mirror, to focus an optical beam by mechanically translating a lens, or extinguish an unwanted optical beam by physically blocking its path. Recent independent developments in microelectromechanical (MEM) devices promise to remedy the issue of high cost and unreliability associated with the "moving parts" needed for these optical functions. This article describes some aspects of these recent developments undertaken in the "microphotronics" group at U.C. Berkeley led by Prof. Richard Muller and the author and comprised of nearly a dozen past and present students and postdoctoral researchers.

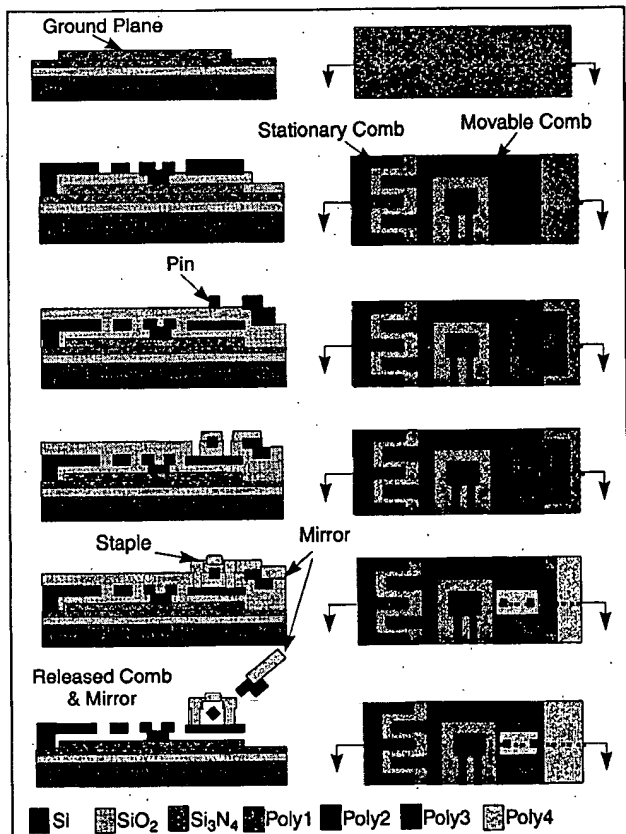
The goal is to put entire functioning optical systems on a silicon chip. To date, silicon-based "integrated-optics" technology, which encompasses fabrication of optical waveguides on a silicon substrate, has already progressed to a highly sophisticated level. However, the functionality of silicon integrated optics is not "complete" in that it does not provide beam-manipulation functions such as switching, modulation, scanning—those that can best be performed with mechanical moving parts. As we have argued above, MEM devices are ideal for this purpose because they can be fabricated on silicon using nearly standard fabrication pro-

K.Y. Lau

BEST AVAILABLE COPY



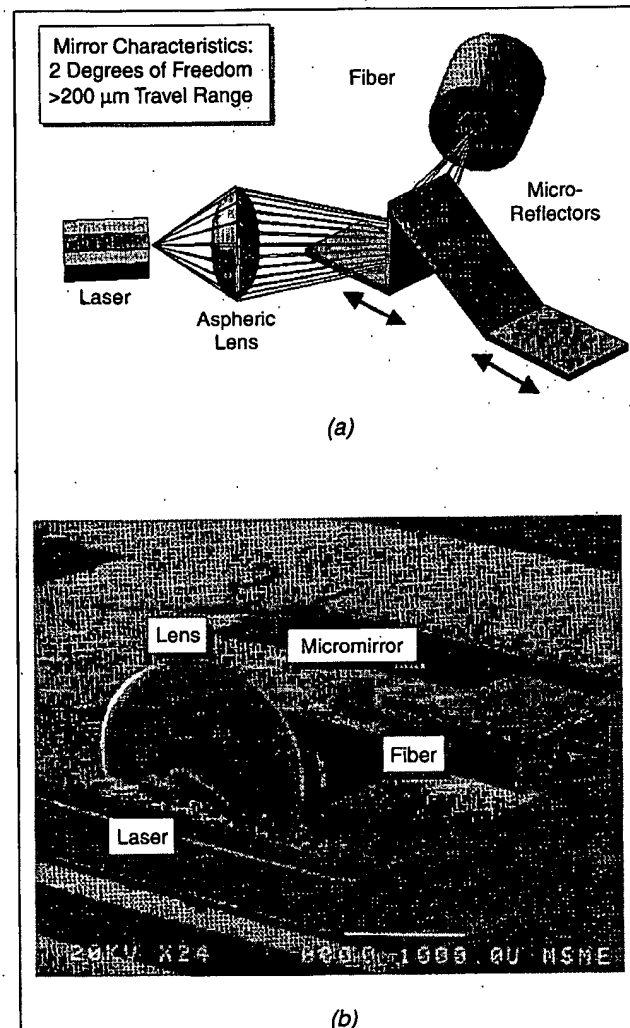
1. Basic micromirror structure for precision alignment of optical components. The size of the mirror measures roughly 200 by 250 μm .



2. Fabrication procedure of a micromirror. It involves a 4-polysilicon process that incorporates the mirror shown in Fig. 1 and the vibromotor actuator described in the text.

cesses, and because photons are massless, which suits MEM devices fine since these microstructures are not designed for delivering forces sizable enough to move bulky objects.

We classify optical MEM devices according to their functionalities: precision optical alignment between components; repetitive beam scanning; and ON/OFF shutter operations. Although the boundaries of these classifications are fuzzy in that devices created for one function can generally be made to perform the



3. (a) Schematic of a laser-to-fiber coupling module showing 2-D optical alignment with two 1-D translational degrees of freedom in the micromirror. (b) SEM photograph of the coupling chip.

others, the classifications are useful for identifying design criteria that are optimized for a particular purpose.

Optical MEM Devices for Precision Alignment

Optical MEM devices designed for precision alignment are aimed at facilitating automated packaging of optoelectronic devices and subsystems, hence substantially lowering the overall production cost of the modules. Examples of these modules include fiber-pigtailed laser transmitters and external-cavity continuously tunable laser diodes. These modules are expensive because they require submicron alignment tolerances that place tight constraints on the positional accuracy of such optoelectronics components as lasers, lenses, gratings, and fibers.

Silicon-optical-bench (SOB) technology commonly used to align optical systems on a silicon substrate, which uses etched v-grooves, solder bumps, and other IC-process-derived techniques to achieve $\pm 1 \mu\text{m}$ transverse alignment [1, 2], is insufficient for high-performance modules. Instead, we promote a paradigm in which SOB technology—a hands-off automated

process—is used for initial placement of the various optical components in the module, followed by an automated active alignment procedure using micromirrors that are prefabricated on the silicon substrate using MEMS technology [3, 4].

A movable micromirror we have developed is shown in Fig. 1. It consists of four polysilicon plates, interconnected by three sets of microhinges [5]. The two end plates can slide linearly and independently on the silicon substrate surface, confined by hubs on the sides. This arrangement provides the mirror with rotational and translational freedom of motion, and a high vertical aspect ratio in its operating position.

The fabrication process for the basic micromirror is shown in Fig. 2. Three $2\text{ }\mu\text{m}$ structural polysilicon layers compose the sliders, hinges, and mirror plates. Sacrificial silicon dioxide films are used as spacers between the structural layers. Upon completion of the surface micromachining process, the alignment grooves for the fiber and lens are etched in KOH. A fourth polysilicon layer is needed for fabrication of the motor drive, which will be described in greater detail below. Finally the sacrificial oxide is dissolved in a concentrated hydrofluoric acid solution and a gold layer is evaporated to increase reflectivity.

A Single-Mode-Fiber Laser Transmitter Module

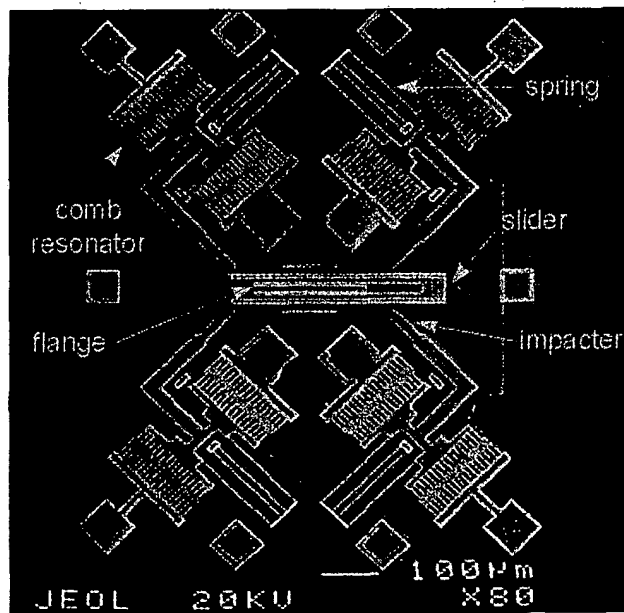
To be specific, we consider a laser-to-fiber coupling module as illustrated schematically in Fig. 3(a). An actual picture of the assembled coupling module is shown in Fig. 3(b). An aspheric microlens was used to image the output of a laser diode into a single-mode fiber. A polysilicon micromirror with two degrees of freedom (linear displacement and angular position) reflects the laser beam at a 45° angle and provides the fine alignment. The lens, laser, and fiber are positioned passively on the substrate using etched alignment grooves and photolithographically defined alignment aids, and they are held in place by low-viscosity epoxy. The height of the fiber core is controlled by mounting it in a silicon subcarrier that is attached to the foundation substrate. Using these techniques, the axial displacement and tilt of the optical components can be minimized, and the reduction in coupling efficiency resulting from these sources of misalignment is negligible. Transverse misalignment of the laser and lens, however, has a significant effect on the coupling, particularly because of the magnification of the lens system. As a consequence of our simple passive-alignment method, the transverse offsets of the laser and lens are on the order of $5\text{-}10\text{ }\mu\text{m}$, which, magnified by the lens, lead to roughly a $20\text{-}40\text{ }\mu\text{m}$ displacement of the beam on the fiber plane. Therefore, the micromirror must have sufficient travel range to compensate for these offsets.

Vibromotor Actuation

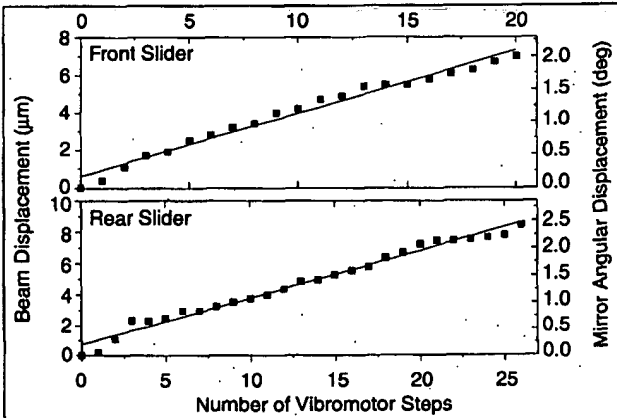
On-chip actuation is necessary in order for the micromachined components to function in a self-contained optical module. Numerous ways exist for on-chip actuation of microstructures; however, actuation of micromirrors for optical alignment purposes will need both precision and range—involving mecha-



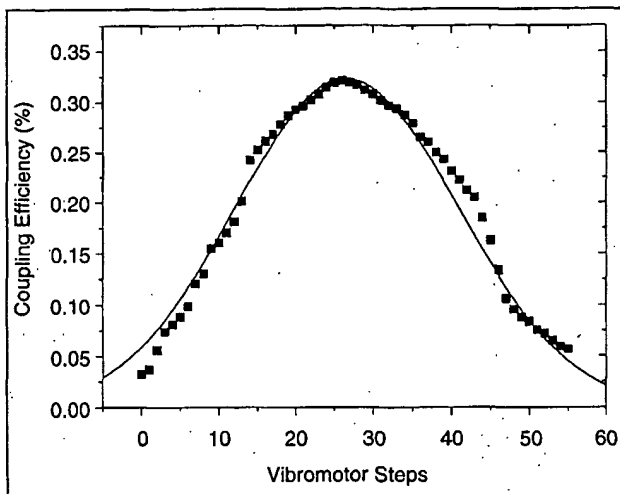
4. Complete self-actuated micromirror. Two sets of vibromotors, comprising 4 comb drives each, drive the front and rear sliders for actuation of the mirror.



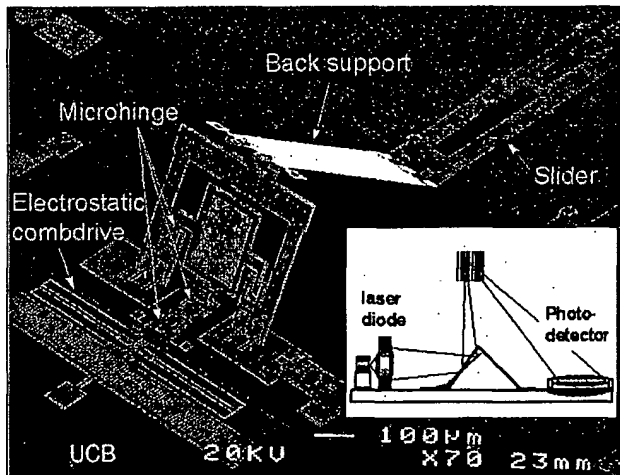
5. Detailed top view of the vibromotor.



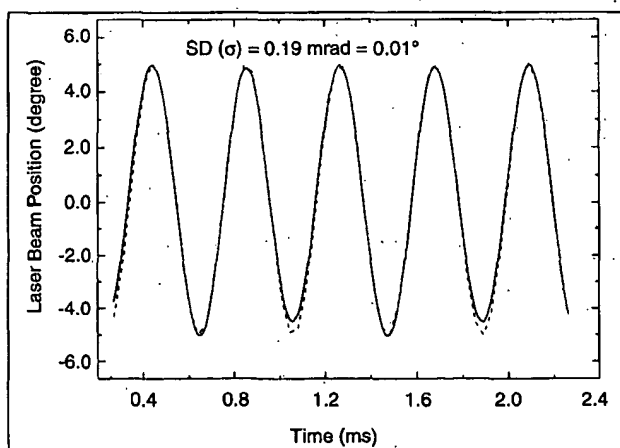
6. Optical beam displacement at the fiber plane as a function of the number of drive steps applied to the vibromotor, for the front and rear slider, respectively.



7. Coupling efficiency from semiconductor laser to single-mode fiber using the actuated micromirror. A peak efficiency of 32% was achieved.



8. SEM photograph of the resonant scanner. An electrostatic comb drive is attached to the bottom of the scanning micromirror. The inset shows a prototype design for an integrated barcode-scanner module on a silicon substrate.



9. The scanning laser-beam position as a function of time (solid curve). The scanner is driven on-resonance by a pure sinusoidal voltage 24 V in amplitude. The dotted curve is a pure sine-wave that fits the measurements with a calculated standard deviation of 0.01° over 18° of scan angle.

nisms reminiscent of stepping motors. Here, we describe a specific type of motor that has been successfully employed to drive micromirrors with submicron precision and with hundreds of microns in range.

As shown in Fig. 4, each of the two sliders is actuated with an integrated microvibromotor [6], which consists of four electrostatic-comb resonators with attached impact arms driving a slider through oblique impact. (The micromirror shown in Fig. 4 is similar to that shown in Fig. 1 except that the front sliding plate is folded under the back-support to save space.) Figure 5 shows a detailed top view of the vibromotor. To balance the forces, two opposing impacters are used for each direction of travel. The resonator is a capacitively driven mass anchored to the substrate through a folded beam flexure. The spring constant of the flexure determines the resonant frequency and travel range of the resonator. The force exerted by the comb drive is proportional to the square of the applied voltage. The comb structures are driven at their resonance frequency (roughly 7.5–8.5 kHz), thereby achieving an amplification of the electrostatic force by the resonator quality factor (typically 30 to 100 in air [6, 7]).

Since energy is transferred to the slider only during impact (typically lasting only a few microseconds), the impacters can deliver short-duration forces that are large enough to overcome static friction in the sliders and hinges. When driven with a free-running resonant oscillation, the slider reaches a maximum velocity of over 1 mm/s. When driven by bursts of RF whose length is adjusted such that only one impact occurs per RF burst, the vibromotor functions like a stepping motor. The amount of motion generated per step is governed by the impact force, the relative masses of the impact arm and the slider, and most important of all, the friction between the slider and the substrate. Once the slider is in position, it is kept in place by static friction until further actuation. Similar structures were previously subjected to shock and vibration tests and showed no detectable slider motion at forces up to 500 G's [3].

To measure the precision of the actuated microreflector, a HeNe laser is reflected from the micromirror surface onto a CCD camera. For the device tested, the average step size was 0.35 μ m for the front slider and 0.42 μ m for the rear slider, with standard deviations of 0.32 μ m and 0.60 μ m respectively (Fig. 6). These deviations are due primarily to the "play" in the hinges and the wobble in the slider structure, as well as the statistical nature of dynamic friction between the slider and substrate. The greater length of the rear slider results in increased wobble and leads to a greater standard deviation.

Next the microreflector was used in a fiber-coupler configuration to provide fine alignment between a semiconductor laser and a single-mode optical fiber (9 μ m core). The light from a standard telecommunications-grade 1.3 μ m DFB laser was imaged by a lens system onto the fiber facet. The actuated microreflector was positioned between the lens and the fiber to provide fine alignment. The microreflector was actuated to provide maximum coupling. Figure 7 shows the dependence of the cou-

pling efficiency on the number of rear vibromotor steps. The step size can be varied by changing the drive voltage to provide various degrees of control. The data show a good fit to a Gaussian curve with deviations being due to slider wobble and angular misalignment of the components. The coupling efficiency was limited to 32% in this arrangement due to the "soft-focusing" optical arrangement; a tighter focus at the fiber plane will produce a higher coupling efficiency, but is less forgiving in beam misalignment. As seen from Fig. 7, the step size in the actuated micromirror is sufficiently small to actually handle a much tighter focus than what is being shown, thus a much higher coupling efficiency, in the 60-80% range, can readily be achievable with a more aggressive optical design.

Optical MEM Devices for Beam Scanning

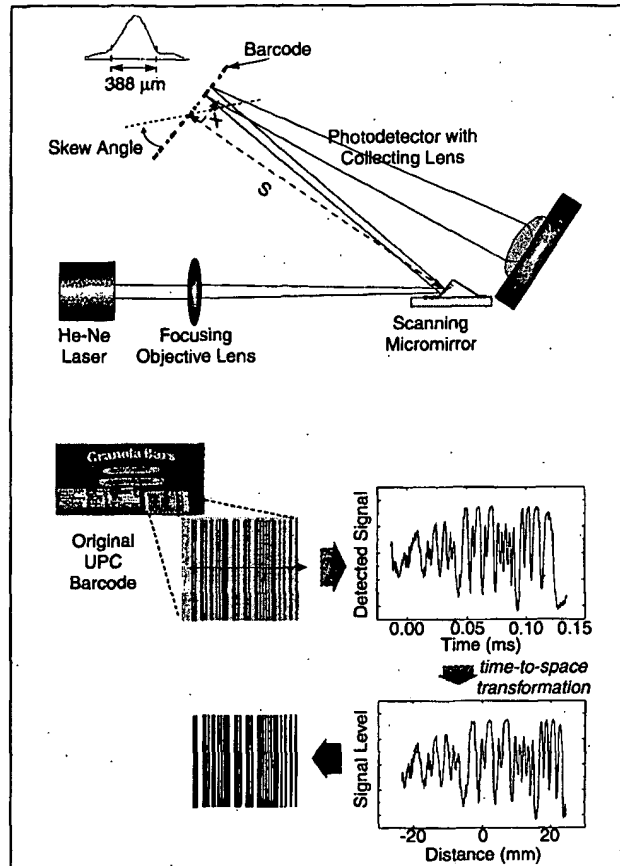
While the micromirrors described above exhibit excellent precision and range in their motions, they are clearly not meant for rapid, repetitive scanning applications such as laser imaging and displays, laser surgery tools, or home-office appliances such as facsimile machines and printers. Barcode scanners are widely used for automatic object identification in many industries. Silicon surface-micromachined scanning micromirrors clearly have advantages compared to bulk, galvanometric-type or rotating-polygon-type scanning mirrors, owing to a fast scan rate, a large scan angle, low mass, and low operating power. More importantly, the integration of the scanner optics, driving motor, and processing electronics onto a single silicon chip can be carried out as part of the fabrication process, greatly reducing assembly cost and improving system reliability.

The diagram inserted in Fig. 8 is a conceptual sketch of an integrated barcode reader system built on a silicon chip. The barcode reader makes use of a silicon surface-micromachined microscanner, which is shown in Fig. 8 [8]. Others have proposed different microscanner designs [5, 9] to be used for optical scanning, but the scanned image resolution is limited by the diffraction from the largest optical aperture in the scanner. As a result, mirrors with dimensions in the hundreds of μm range are necessary for practical optical-scanning systems. In order to create high-aspect-ratio optical surfaces, we use the microhinge technology described above, which permits the micromirrors to be folded out of the plane of the substrate after planar processing is completed. Using this folding technology, we have fabricated electrostatic comb-driven scanning micromirrors that have apertures large enough to build barcode-reading systems.

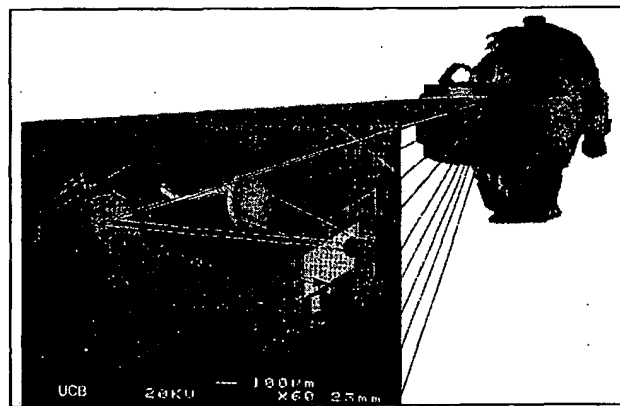
Barcode Reader on a Chip

As shown in the SEM micrograph in Fig. 8, the size of the mirror is 200 by 250 μm , and the shafts around which the mirror pivots are 160 μm below the top of the mirror. The micromirror is inclined at 60° to the substrate and is supported by a hinged slider at its back.

An electrostatic comb drive is used to actuate this scanner. These comb drives are similar to those used in the vibromotor described above, except that the mirror is now directly linked to

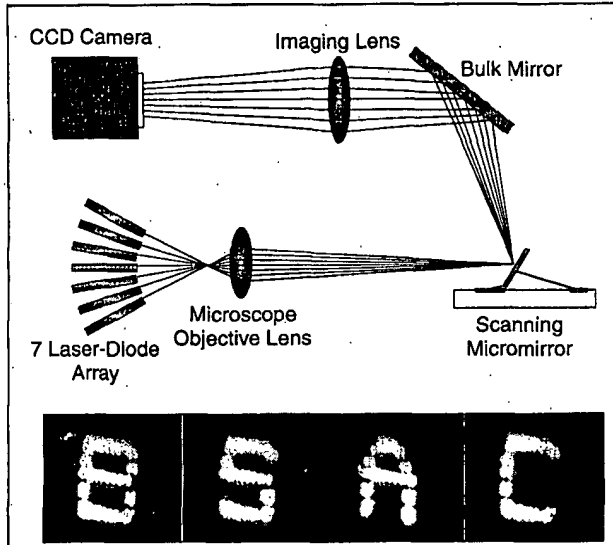


10. (a) Schematic of the experimental setup for microscanner characterization and barcode-reading. The focal length of the objective lens is 45 mm, and $S = 50$ mm for the barcode scanning experiment. The inset is the beam profile of the scanning laser spot measured at the barcode. (b) Results of the barcode scanning experiment. The original UPC barcode used is shown in the upper-left corner, and the detected time signal is transformed into a spatial one. The reconstructed barcode symbol is shown in the lower-left-hand corner.



11. A 2-D head-mounted raster-scanning design using two orthogonal scanning micromirrors on a chip.

the comb drive, instead of being actuated through an impact arm. The maximum excursion of the shuttle from its rest position is determined by the length of the comb fingers, which, in this design, is 20 μm . This results in a 7.6° rotation of the mirror. Therefore, the maximum scan angle of this resonant scanner is



12. Scanning-display demonstration using a 1-D scanning micromirror and a 7-element individually addressable laser-diode array.

roughly 15° (30° optical). This compares favorably with angles typically achieved in bulk resonant scanners [10].

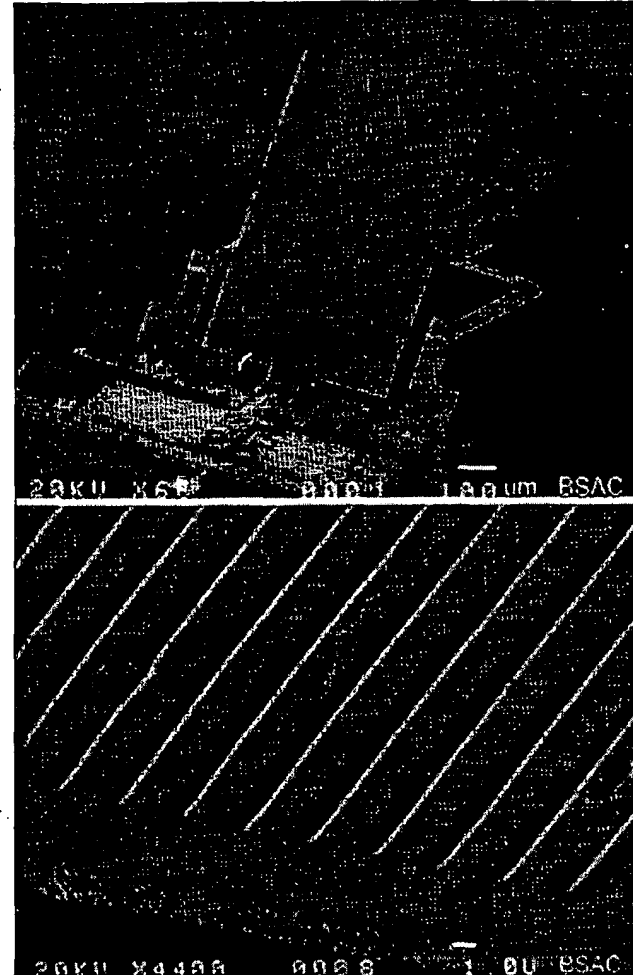
One important issue for barcode readers is the scan repeatability. To determine the accuracy of the microscanner line scan, the position of the scanning laser beam was recorded with a position-sensing detector. Figure 9 shows the scanning laser-beam position as a function of time when the scanner is driven harmonically using a 30 V (amplitude) ac voltage at 3 kHz. The dotted curve is a sinusoid fitted to the measured data. The standard deviation of $8.3 \mu\text{m}$ (0.01°) over the 15-mm scan (18° in scan angle) translates into a scan jitter of $18 \mu\text{m}$, or 9% of the thinnest bars—200- μm wide, at the image plane.

We employed the experimental setup depicted in Fig. 10(a) to demonstrate barcode scanning using the electrostatic comb-driven micromirror. For simplicity, the post-objective scanning scheme was adopted so that no flat-field lens was needed. The distortion introduced by mapping a nonplanar image plane to a flat image surface (the barcode) is not a concern as long as the depth-of-field of the optical system is sufficiently large such that the spot size at the barcode is always small enough to resolve the thinnest bars. The comb drive is driven at its resonant frequency of approximately 3 kHz. The universal product code (UPC) barcode from a commercial product is used in our barcode-reading experiment. Figure 10(b) shows the recorded signal and the reconstructed barcode pattern.

Micro-Raster-Scanning Display

Single-mirror scanners can be combined to form more complicated microscanners such as a two-mirror, two-axis raster scanner that can be used to build a compact display system. An illustration of such an integrated-microdisplay, head-mounted module is shown in Fig. 11.

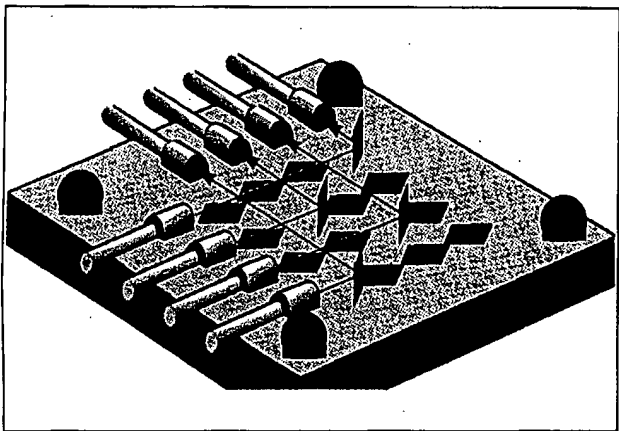
To demonstrate a scanning-laser display, a system setup as sketched in Fig. 12 is used [11]. All seven beams from the indi-



13. Scanning diffraction-grating. The bottom photo shows detailed grating structure.

vidually addressable laser array are collected by a single microscope objective by focusing the central point of the fan onto the micromirror. The system has a resolution of 7×11 pixels, which is determined by the number of lasers (vertically), the divergence angle of the laser beam, the physical layout of the fan-lasers, and the size and scan angle of the mirror (laterally). Displayed in Fig. 12 are four individual characters (BSAC) generated by this laser-scanning system.

So far, the only optical element we have described is a plane mirror. Obviously, optical elements of higher functionality, such as diffraction gratings and fresnel lens, can be fabricated on these surfaces using the same processing techniques employed to create the microstructures. As an example, Fig. 13 shows an actuated diffraction grating using a foundry surface-micromachining process (Multi-User MEMS ProcesS, or MUMPS, at MCNC, a MEM foundry in North Carolina). Rectangular gratings with $4 \mu\text{m}$ period and 0.75 mm depth are produced on a $500 \times 1000 \mu\text{m}$ polysilicon plate that is mounted on torsion bars and actuated by an electrostatic comb drive [12]. Operated as a first-order reflective grating, it can be used to build an integrated scanning microspectrometer with a resolving



14. *NxN* nonblocking fiber-optic crossbar-switch implementation using a "mirror farm" on a silicon chip.

power of 250, or, as a grating demultiplexer for multichannel wavelength-division-multiplexed optical networks.

MEM-Based Optical Switches

A different class of optical functions involves on/off switching of optical beams. There are numerous examples of how they can be implemented, including sliding of an erected mirror in and out of paths of optical beams to produce switching functions [13]. The ultimate implementation in this category of devices is an $N \times N$ nonblocking fiber-optic cross-bar switch in which the collimated optical beam from any one of the N input fibers can be directed to any one of the N output fibers by selective actuation of a "mirror farm" (Fig. 14) [14]. The individual mirrors are hinged to the substrate in manners similar to the torsional hinges described above and can be rotated out of the plane of the substrate to a vertical position. There is no need for continuous control of the intermediate position of the mirror; however, the vertical stop-position must be extremely precise or else the coupling of the reflected beam to the output fiber will be unacceptably poor. Rough estimates put the angular accuracy of the mirror in its vertical position to within $< 5^\circ$, which is challenging indeed. Some form of built-in mechanical stop [14] must be applied consistently over the entire mirror farm in order for the switch to meet the optical insertion loss required for network implementations.

Similar to other optical microstructures described above, many ways to provide the actuation force exist. One recently developed actuation mechanism involves plating the micro-mirrors with a magnetic material so that they can be actuated with an external magnetic field [15]. The disadvantage of an external actuation field is the difficulty in localizing the field to produce individual, independent actuation of the mirrors. One way to overcome this problem is to incorporate "electrostatic hold-down" in the mirror design, so that only the mirrors not held-down can be rotated to the vertical, "ON" position [16]. Alternatively, local wire-loop can be fabricated on the mirror whereby a local magnetic field can be selectively generated by passing a current through the loop. The amount of current needed causes heating of the mirror that may deform it by an

amount that significantly affects the optical performance of the device—even small deformations on the order of a fraction of an optical wavelength suffices to produce significant consequences in some applications. Such issues are still currently under investigation [17].

Looking Forward

We have not mentioned a very significant development in optical MEM technology that has emerged in recent years and is by far the biggest commercial application of MEM technology to date—that of the digital micromirror display (DMD), developed and commercialized by Texas Instruments. It uses rotating mirrors as optical ON/OFF elements in individual pixels of a projection display. It wins hands-down in a "video shoot-out" over alternative projection display technologies. It involves superb engineering of a single optical MEM element, repeated reliably and economically a millions times over, on a silicon chip measuring approximately 1×2 cm in size. The type of optical MEM devices we described above are at the same time more and less ambitious than that of the DMD, in that only a small number of MEM elements are involved, but they are called upon to perform more precise functions. The goal of these pursuits is to develop a generic enabling technology upon which future optical systems are based, advancing beyond the all-important and yet function-specific technologies such as DMD. It is tempting to produce MEM versions of bulk optomechanical devices in the general forms that have proven to be indispensable in optics laboratories the world over in the last couple of decades [18]. Future developments and successes of optical MEM technology may well be determined by functional-specific elements that take the best advantage of what MEM technology can offer for those specific applications.

Acknowledgments

The work described in this article represents the collective accomplishments of the "first generation" students and postdoctoral fellows at U.C. Berkeley who initiated and grew the microphotonics program over the last three years. They include: M. Daneman, A. Friedberger, J. Judy, M.H. Kiang, O. Solgaard, and N. Tien. See Reference section below for a sample of articles they have written during this period.

Kam Y. Lau is a professor in the University of California at Berkeley's Department of Electrical Engineering and Computer Science in Berkeley, California.

References

1. M.S. Cohen, M.F. Cina, E. Bassous, M.M. Opyrsko, J.L. Speidell, et al., "Packaging of High-Density Fiber/Laser Modules Using Passive Alignment Techniques," *IEEE Trans. on Components, Hybrids, and Manuf. Tech.*, vol. 15, (6), pp. 944-954, December 1992.
2. M.J. Wale and C. Edge, "Self-aligned flip-chip assembly of photonic devices with electrical and optical connections," *IEEE Trans. on Components, Hybrids, and Manuf. Tech.*, vol. 13, (4), pp. 780-786, December 1990.
3. O. Solgaard; M. Daneman, N. Tien, A. Friedberger, R.S. Muller, and K.Y. Lau, "Optoelectronic packaging using silicon surface-micromachined

Excellence in Electronics

Linear Electric Actuators and Generators

I. Boldea and Syed A. Nasar

This book presents the first unified treatment of the subject, including the construction, operation, control, and design of LEAs and LEGs. Chapters describe linear induction, permanent-magnet, linear reluctance, switched reluctance, and linear stepper actuators, as well as various types of linear electric generators. The text is amply illustrated with numerous design examples.

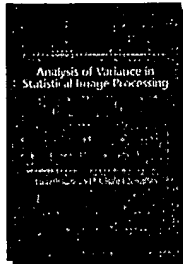
1997 247 pp. 48017-5 Hardback \$59.95

Analysis of Variance in Statistical Image Processing

Ludwik Kurz and M. Hafed Bentefifa

The authors present a number of computationally efficient algorithms and techniques to deal with such problems as line, edge, and object detection, as well as image restoration and enhancement. By describing the basic principles of these techniques, and showing their use in specific situations, the book will facilitate the design of new algorithms for particular applications.

1997 223 pp. 58182-6 Hardback \$49.95



Applied Neural Networks for Signal Processing

Fa-Long Luo and Rolf Unbehauen

Luo and Unbehauen cover the basic principles and models of neural networks in signal processing and discuss a number of powerful algorithms and architectures for a range of important problems, including practical implementation procedures. A key feature of the book is that many carefully designed simulation examples are included to help guide the reader in the development of systems for new applications.

1997 c.400 pp. 56391-7 Hardback \$69.95

Engineering Ethics

Balancing Cost, Schedule, and Risk—Lessons Learned from the Space Shuttle

Rosa Lynn B. Pinkus,

Larry J. Shuman,

Norman P. Hummon, and

Harvey Wolfe

The authors consider the design and development of the main engines of the space shuttle as a paradigm for how individual engineers perceive, articulate, and resolve ethical dilemmas in a large, complex organization.

1997 397 pp. 43171-9 Hardback \$69.95
43750-4 Paperback \$27.95



Introduction to Optical Engineering

Francis T.S. Yu and Xiangyang Yang

The authors present basic optical principles, particularly reflection, refraction, aberrations, diffraction and interference. They discuss a wide variety of optical devices and processes, including simple optical instruments, photodetectors, spatial light modulators, holography and lasers. The book includes many worked examples and over 250 problems.

1997 423 pp. 57366-1 Hardback \$110.00
57493-5 Paperback \$44.95

Available in
bookstores or from

CAMBRIDGE
UNIVERSITY PRESS

40 West 20th Street, New York, NY 10011-4211

Call toll-free 800-872-7423. Web site: <http://www.cup.org>
MasterCard/VISA accepted. Prices subject to change.

alignment mirrors," *IEEE Photonics Technology Letters*, vol. 7, (1), pp. 41-43, January 1995.

4. M.J. Daneman, O. Solgaard, N.C. Tien, K.Y. Lau, and R.S. Muller, "Laser-to-fiber coupling module using a micromachined alignment mirror," *Photon. Tech. Lett.*, vol. 8, no. 3, pp. 396-8, 1996.

5. K.S.J. Pister, M.W. Judy, S.R. Burgett, and R.S. Fearing, "Microfabricated hinges," *Sensors and Actuators (A)*, vol. 33, (3), 1992, pp. 249-256.

6. A.P. Lee, D.J. Nikkel Jr., and A.P. Pisano, "Polysilicon linear vibromotors", 7th International Conference on Solid-state Sensors and Actuators, 1993, pg. 46-47; W.C. Tang T.-C. H. Nguyen, M.W. Judy, and R.T. Howe, "Electrostatic-comb drive of lateral polysilicon resonators," *Sensors and Actuators*, vol. A21-23, 1990, pp. 328-331; M.J. Daneman, N.C. Tien, O. Solgaard, A.P. Pisano, K.Y. Lau and R.S. Muller, "Linear vibromotor for positioning optical components," *IEEE J. Microelectromechanical Systems*, vol. 5, no. 3, pp. 159-65, 1996.

7. Y.H. Cho, A.P. Pisano, and R.T. Howe, "Viscous Damping Model for Laterally Oscillating Microstructures," *Journal of Microelectromechanical Systems*, vol. 3, no. 2, 1994, pp. 81-87.

8. M.H. Kiang, O. Solgaard, R.S. Muller, and K.Y. Lau, "Micromechanical polysilicon micromirrors for barcode readers," *IEEE Photon. Tech. Letts.*, vol. 8, no. 12, pp. 1707-09, 1996.

9. A. Yasseen, S. W. Smith, M. Mehregany, and F. L. Merat, "Diffraction gratings scanners using polysilicon micromotors," in *Proceed. IEEE Micro Electro Mechanical Systems Workshop*, pp. 175-180, Amsterdam, the Netherlands, Jan. 1995.

10. J.I. Montagu, in *Optical Scanning*, edited by G. F. Marshall, Marcel Dekker, Inc., New York, NY, 1991, chap. 10.

11. M.H. Kiang, D.A. Francis, C.J. Chang-Hasnain, K.Y. Lau, and R.S. Muller, "Actuated polysilicon mirror for raster-scanning display", *Transducers 97*, Chicago, June 1997.

12. M.H. Kiang, K.Y. Lau and R.S. Muller, "Surfaced-micromachined diffraction gratings for scanning spectrometer application", *Transducers 97*, Chicago, June 1997.

13. M.C. Wu, L.Y. Lin, S.S. Lee and K.S.J. Pister, "Micromachined free-space integrated micro-optics," *Sensors and Actuators A*, vol. 50, pp. 127-134, 1995.

14. H. Toshiyoshi and H. Fujita, "Electrostatic micro torsional mirrors for an optical switch matrix," *IEEE J. Microelectromechanical Systems*, vol. 5, no. 4, pp. 231-237, 1996.

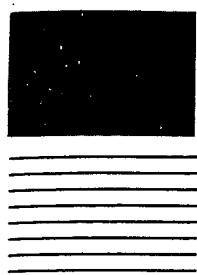
15. J.W. Judy, R.S. Muller, and H. Zappe, "Magnetic micro-actuation of polysilicon flexure structures," *IEEE J. Microelectromechanical Systems*, vol. 4, no. 4, pp. 162-164, 1995.

16. J.W. Judy and R.S. Muller, "Batch-fabricated, addressable magnetically actuated microstructures," *Tech. Digest. Solid State Sensors and Actuators Workshop*, Hilton Head 1996, Hilton Head Island, S. Carolina, June 1996, pg. 187-90.

17. R.A. Miller, G.W. Burr, Y.C. Tai, and D. Psaltis, "Magnetically actuated micromirrors for use as optical deflectors", *Proceed. Of 4th International Symposium on magnetic materials, processes and devices*, Chicago, Oct. 1995, Ed. C.T. Romankiv, D.A. Herman Jr., Pennington, N.J., Electrochem. Society, 1996, pp. 474-81.

18. L.Y. Lin, J.L. Shen, S.S. Lee, and M.C. Wu, "Surface-micromachined micro-xyz stages for free-space microoptical bench", *IEEE Photon. Tech. Letts.*, vol. 9, no. 3, pp. 345-7, 1997.

CD



OPTICS

SECOND EDITION

EUGENE HECHT
Adelphi University

With Contributions by Alfred Zajac



ADDISON-WESLEY PUBLISHING COMPANY
Reading, Massachusetts • Menlo Park, California • Don Mills, Ontario
Wokingham, England • Amsterdam • Sydney • Singapore
Tokyo • Madrid • Bogotá • Santiago • San Juan

path SQP traversed by a ray would then be a relative minimum. At the other extreme, if the mirrored surface conformed to a curve lying within the ellipse, like the dashed one shown, that same ray along SQP would now negotiate a relative maximum OPL. This is true even though other unused paths (where $\theta_i \neq \theta_r$) would actually be shorter (i.e., apart from inadmissible curved paths). Thus in all cases the rays travel a stationary OPL in accord with the reformulated Fermat's principle. Note that since the principle speaks only about the path and not the direction along it, a ray going from P to S will trace the same route as one from S to P . This is the very useful *principle of reversibility*.

Fermat's achievement stimulated a great deal of effort to supersede Newton's laws of mechanics with a similar variational formulation. The work of many men, notably Pierre de Maupertuis (1698–1759) and Leonhard Euler, finally led to the mechanics of Joseph Louis Lagrange (1736–1813) and hence to the *principle of least action*, formulated by William Rowan Hamilton (1805–1865). The striking similarity between the principles of Fermat and Hamilton played an important part in Schrödinger's development of quantum mechanics. In 1942 Richard Phillips Feynman (b. 1918) showed that quantum mechanics can be fashioned in an alternative way using a variational approach. The continuing evolution of variational principles brings us back to optics via the modern formalism of quantum optics (see Chapter 13).

Fermat's principle is not so much a computational device as it is a concise way of thinking about the propagation of light. It is a statement about the grand scheme of things without any concern for the contributing mechanisms, and as such it will yield insights under a myriad of circumstances.

4.3 THE ELECTROMAGNETIC APPROACH

Thus far we have been able to deduce the laws of reflection and refraction using three different approaches: *Huygens's principle*, the *theorem of Malus and Dupin*, and *Fermat's principle*. Each yields a distinctive and valuable point of view. Yet another and even more powerful approach is provided by the electromagnetic

theory of light. Unlike the previous techniques, which say nothing about the incident, reflected, and transmitted radiant flux densities (i.e., I_i , I_r , I_t , respectively), the electromagnetic theory treats these within the framework of a far more complete description.

The body of information that forms the subject of optics has accrued over many centuries. As our knowledge of the physical universe becomes more extensive, the concomitant theoretical descriptions must become ever more encompassing. This, quite generally, brings with it an increased complexity. And so, rather than using the formidable mathematical machinery of the quantum theory of light, we will often avail ourselves of the simpler insights of simpler times (e.g., Huygens's and Fermat's principles). Thus even though we are now going to develop another and more extensive description of reflection and refraction, we will not put aside those earlier methods. In fact, throughout this study we shall use the simplest technique that can yield sufficiently accurate results for our particular purposes.

4.3.1 Waves at an Interface

Suppose that the incident monochromatic lightwave is planar, so that it has the form

$$\mathbf{E}_i = \mathbf{E}_{0i} \exp [i(\mathbf{k}_i \cdot \mathbf{r} - \omega_i t)] \quad (4.11)$$

or, more simply,

$$\mathbf{E}_i = \mathbf{E}_{0i} \cos (\mathbf{k}_i \cdot \mathbf{r} - \omega_i t). \quad (4.12)$$

Assume that \mathbf{E}_{0i} is constant in time, that is, the wave is linearly or plane polarized. We'll find in Chapter 8 that any form of light can be represented by two orthogonal linearly polarized waves, so that this doesn't actually represent a restriction. Note that just as the origin in time, $t = 0$, is arbitrary, so too is the origin O in space, where $\mathbf{r} = 0$. Thus, making no assumptions about their directions, frequencies, wavelengths, phases, or amplitudes, we can write the reflected and transmitted waves as

$$\mathbf{E}_r = \mathbf{E}_{0r} \cos (\mathbf{k}_r \cdot \mathbf{r} - \omega_r t + \epsilon_r) \quad (4.13)$$

and

$$\mathbf{E}_t = \mathbf{E}_{0t} \cos (\mathbf{k}_t \cdot \mathbf{r} - \omega_t t + \epsilon_t). \quad (4.14)$$

Here ϵ_r and ϵ_t are *phase constants* relative to \mathbf{E}_i and are introduced because the position of the origin is not unique. Figure 4.19 depicts the waves in the vicinity of the planar interface between two homogeneous lossless dielectric media of indices n_i and n_t .

The laws of electromagnetic theory (Section 3.1) lead to certain requirements that must be met by the fields, and these are referred to as the boundary conditions. Specifically, one of these is that the component of the electric field intensity \mathbf{E} that is tangent to the interface must be continuous across it (the same is true for \mathbf{H}). In other words, the total tangential component of \mathbf{E} on one side of the surface must equal that on the other (Problem 4.22). Thus since $\hat{\mathbf{u}}_n$ is the unit vector normal to the interface, regardless of the direction of the electric field within the wavefront, the cross-product of it with $\hat{\mathbf{u}}_n$ will be perpendicular to $\hat{\mathbf{u}}_n$ and therefore tangent to the interface. Hence

$$\hat{\mathbf{u}}_n \times \mathbf{E}_i + \hat{\mathbf{u}}_n \times \mathbf{E}_r = \hat{\mathbf{u}}_n \times \mathbf{E}_t \quad (4.15)$$

or

$$\begin{aligned} & \hat{\mathbf{u}}_n \times \mathbf{E}_{0i} \cos(\mathbf{k}_i \cdot \mathbf{r} - \omega_i t) \\ & + \hat{\mathbf{u}}_n \times \mathbf{E}_{0r} \cos(\mathbf{k}_r \cdot \mathbf{r} - \omega_r t + \epsilon_r) \\ & = \hat{\mathbf{u}}_n \times \mathbf{E}_{0t} \cos(\mathbf{k}_t \cdot \mathbf{r} - \omega_t t + \epsilon_t). \end{aligned} \quad (4.16)$$

This relationship must obtain at any instant in time and at any point on the interface ($y = b$). Consequently, \mathbf{E}_i , \mathbf{E}_r , and \mathbf{E}_t must have precisely the same functional dependence on the variables t and r , which means that

$$\begin{aligned} (\mathbf{k}_i \cdot \mathbf{r} - \omega_i t)|_{y=b} &= (\mathbf{k}_r \cdot \mathbf{r} - \omega_r t + \epsilon_r)|_{y=b} \\ &= (\mathbf{k}_t \cdot \mathbf{r} - \omega_t t + \epsilon_t)|_{y=b}. \end{aligned} \quad (4.17)$$

With this as the case, the cosines in Eq. (4.16) cancel, leaving an expression independent of t and r , as indeed it must be. Inasmuch as this has to be true for all values of time, the coefficients of t must be equal, to wit

$$\omega_i = \omega_r = \omega_t. \quad (4.18)$$

Recall that the electrons within the media are undergoing (linear) forced vibrations at the frequency of the incident wave. Clearly, whatever light is scattered has that same frequency. Furthermore,

$$\begin{aligned} (\mathbf{k}_i \cdot \mathbf{r})|_{y=b} &= (\mathbf{k}_r \cdot \mathbf{r} + \epsilon_r)|_{y=b} \\ &= (\mathbf{k}_t \cdot \mathbf{r} + \epsilon_t)|_{y=b}, \end{aligned} \quad (4.19)$$

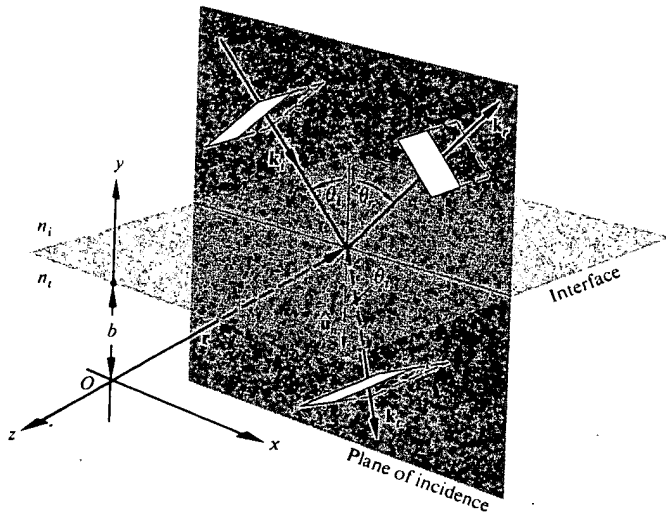


Figure 4.19 Plane waves incident on the boundary between two homogeneous, isotropic, lossless dielectric media.

wherein \mathbf{r} terminates on the interface. The values of ϵ_r and ϵ_t correspond to a given position of O , and thus they allow the relation to be valid regardless of that location. (For example, the origin might be chosen such that \mathbf{r} was perpendicular to \mathbf{k}_i but not to \mathbf{k}_r or \mathbf{k}_t .) From the first two terms we obtain

$$[(\mathbf{k}_i - \mathbf{k}_r) \cdot \mathbf{r}]_{y=b} = \epsilon_r. \quad (4.20)$$

Recalling Eq. (2.42), this expression simply says that the endpoint of \mathbf{r} sweeps out a plane (which is of course the interface) perpendicular to the vector $(\mathbf{k}_i - \mathbf{k}_r)$. To phrase it slightly differently, $(\mathbf{k}_i - \mathbf{k}_r)$ is parallel to $\hat{\mathbf{u}}_n$. Notice, however, that since the incident and reflected waves are in the same medium, $\mathbf{k}_i = \mathbf{k}_r$. From the fact that $(\mathbf{k}_i - \mathbf{k}_r)$ has no component in the plane of the interface, that is, $\hat{\mathbf{u}}_n \times (\mathbf{k}_i - \mathbf{k}_r) = 0$, we conclude that

$$k_i \sin \theta_i = k_r \sin \theta_r;$$

hence we have the law of reflection, that is,

$$\theta_i = \theta_r.$$

Furthermore, since $(\mathbf{k}_i - \mathbf{k}_t)$ is parallel to $\hat{\mathbf{u}}_n$ all three vectors, \mathbf{k}_i , \mathbf{k}_r , and $\hat{\mathbf{u}}_n$, are in the same plane, the plane of incidence. Again, from Eq. (4.19) we obtain

$$[(\mathbf{k}_i - \mathbf{k}_t) \cdot \mathbf{r}]_{y=b} = \epsilon_t, \quad (4.21)$$

and therefore $(\mathbf{k}_i - \mathbf{k}_t)$ is also normal to the interface.

Thus \mathbf{k}_i , \mathbf{k}_r , \mathbf{k}_t , and $\hat{\mathbf{u}}_n$ are all coplanar. As before, the tangential components of \mathbf{k}_i and \mathbf{k}_t must be equal, and consequently

$$k_i \sin \theta_i = k_t \sin \theta_t. \quad (4.22)$$

But because $\omega_i = \omega_t$, we can multiply both sides by c/ω_i to get

$$n_i \sin \theta_i = n_t \sin \theta_t,$$

which is Snell's law. Finally, if we had chosen the origin O to be in the interface, it is evident from Eqs. (4.20) and (4.21) that ϵ_r and ϵ_t would both have been zero. That arrangement, although not as instructive, is certainly simpler, and we'll use it from here on.

4.3.2 Derivation of the Fresnel Equations

We have just found the relationship that exists among the phases of $\mathbf{E}_i(\mathbf{r}, t)$, $\mathbf{E}_r(\mathbf{r}, t)$, and $\mathbf{E}_t(\mathbf{r}, t)$ at the boundary. There is still an interdependence shared by the amplitudes \mathbf{E}_{0i} , \mathbf{E}_{0r} , and \mathbf{E}_{0t} , which can now be evaluated. To that end, suppose that a plane monochromatic wave is incident on the planar surface separating two isotropic media. Whatever the polarization of the wave, we shall resolve its \mathbf{E} - and \mathbf{B} -fields into components parallel and perpendicular to the plane of incidence and treat these constituents separately.

Case 1: \mathbf{E} perpendicular to the plane of incidence. We now assume that \mathbf{E} is perpendicular to the plane of incidence and that \mathbf{B} is parallel to it (Fig. 4.20). Recall that $E = vB$, so that

$$\hat{\mathbf{k}} \times \mathbf{E} = v\mathbf{B} \quad (4.23)$$

and, of course,

$$\hat{\mathbf{k}} \cdot \mathbf{E} = 0 \quad (4.24)$$

(i.e., \mathbf{E} , \mathbf{B} , and the unit propagation vector $\hat{\mathbf{k}}$ form a right-handed system). Again making use of the continuity of the tangential components of the \mathbf{E} -field, we have at the boundary at any time and any point

$$\mathbf{E}_{0i} + \mathbf{E}_{0r} = \mathbf{E}_{0t}, \quad (4.25)$$

where the cosines cancel. Realize that the field vectors

as shown really ought to be envisioned at $y = 0$ (i.e., at the surface), from which they have been displaced for the sake of clarity. Note too that although \mathbf{E}_r and \mathbf{E}_t must be normal to the plane of incidence by symmetry, we are guessing that they point outward at the interface when \mathbf{E}_i does. The directions of the \mathbf{B} -fields then follow from Eq. (4.23).

We will need to invoke another of the boundary conditions in order to get one more equation. The presence of material substances that become electrically polarized by the wave has a definite effect on the field configuration. Thus, although the tangential component of \mathbf{E} is continuous across the boundary, its normal component is not. Instead the normal component of the product $\epsilon\mathbf{E}$ is the same on either side of the

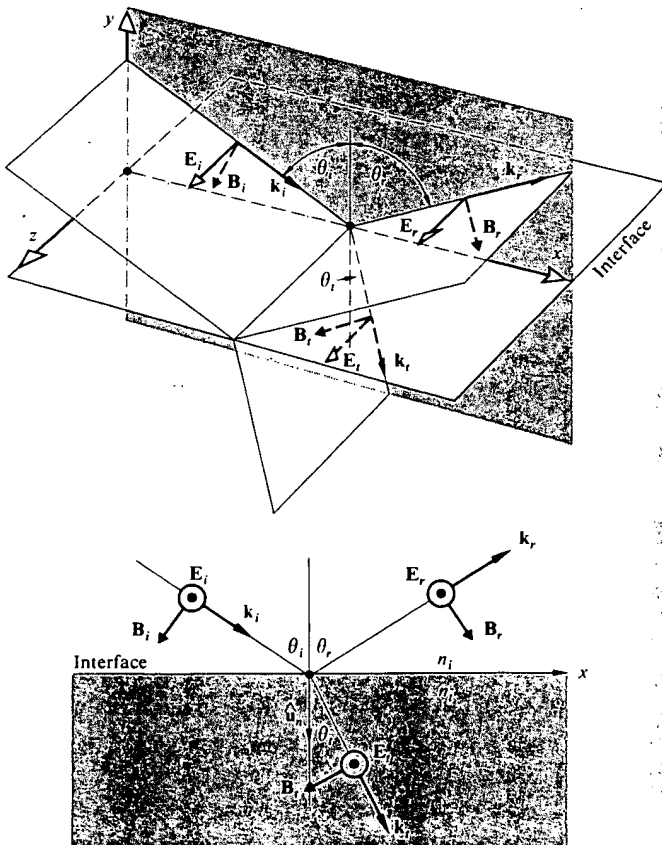


Figure 4.20 An incoming wave whose \mathbf{E} -field is normal to the plane of incidence.

interface. Similarly, the normal component of \mathbf{B} is continuous, as is the tangential component of $\mu^{-1}\mathbf{B}$. Here the effect of the two media appears via their permeabilities μ_i and μ_t . This boundary condition will be the simplest to use, particularly as applied to reflection from the surface of a conductor.* Thus the continuity of the tangential component of \mathbf{B}/μ requires that

$$-\frac{\mathbf{B}_i}{\mu_i} \cos \theta_i + \frac{\mathbf{B}_r}{\mu_i} \cos \theta_r = -\frac{\mathbf{B}_t}{\mu_t} \cos \theta_t, \quad (4.26)$$

where the left and right sides are the total magnitudes of \mathbf{B}/μ parallel to the interface in the incident and transmitting media, respectively. The positive direction is that of increasing x , so that the components of \mathbf{B}_i and \mathbf{B}_t appear with minus signs. From Eq. (4.23) we have

$$B_i = E_i/v_i, \quad (4.27)$$

$$B_r = E_r/v_r, \quad (4.28)$$

and

$$B_t = E_t/v_t. \quad (4.29)$$

Thus since $v_i = v_r$ and $\theta_i = \theta_r$, Eq. (4.26) can be written as

$$\frac{1}{\mu_i v_i} (E_i - E_r) \cos \theta_i = \frac{1}{\mu_t v_t} E_t \cos \theta_t. \quad (4.30)$$

Making use of Eqs. (4.12), (4.13), and (4.14) and remembering that the cosines therein equal one another $y = 0$, we obtain

$$\frac{n_i}{\mu_i} (E_{0i} - E_{0r}) \cos \theta_i = \frac{n_t}{\mu_t} E_{0t} \cos \theta_t. \quad (4.31)$$

Combined with Eq. (4.25), this yields

$$\left(\frac{E_{0r}}{E_{0i}} \right)_{\perp} = \frac{\frac{n_i}{\mu_i} \cos \theta_i - \frac{n_t}{\mu_t} \cos \theta_t}{\frac{n_i}{\mu_i} \cos \theta_i + \frac{n_t}{\mu_t} \cos \theta_t} \quad (4.32)$$

* In keeping with our intent to use only the \mathbf{E} - and \mathbf{B} -fields, at least in the early part of this exposition, we have avoided the usual statements in terms of \mathbf{H} , where

$$\mathbf{H} = \mu^{-1} \mathbf{B}. \quad [A1.14]$$

and

$$\left(\frac{E_{0t}}{E_{0i}} \right)_{\perp} = \frac{2 \frac{n_i}{\mu_i} \cos \theta_i}{\frac{n_i}{\mu_i} \cos \theta_i + \frac{n_t}{\mu_t} \cos \theta_t}. \quad (4.33)$$

The \perp subscript serves as a reminder that we are dealing with the case in which \mathbf{E} is perpendicular to the plane of incidence. These two expressions, which are completely general statements applying to any linear, isotropic, homogeneous media, are two of the **Fresnel equations**. Quite often one deals with dielectrics for which $\mu_i \approx \mu_t \approx \mu_0$; consequently the most common form of these equations is simply

$$r_{\perp} \equiv \left(\frac{E_{0r}}{E_{0i}} \right)_{\perp} = \frac{n_i \cos \theta_i - n_t \cos \theta_t}{n_i \cos \theta_i + n_t \cos \theta_t} \quad (4.34)$$

and

$$t_{\perp} \equiv \left(\frac{E_{0t}}{E_{0i}} \right)_{\perp} = \frac{2 n_i \cos \theta_i}{n_i \cos \theta_i + n_t \cos \theta_t}. \quad (4.35)$$

Here r_{\perp} denotes the **amplitude reflection coefficient**, and t_{\perp} is the **amplitude transmission coefficient**.

Case 2: \mathbf{E} parallel to the plane of incidence. A similar pair of equations can be derived when the incoming \mathbf{E} -field lies in the plane of incidence, as shown in Fig. 4.21. Continuity of the tangential components of \mathbf{E} on either side of the boundary leads to

$$E_{0i} \cos \theta_i - E_{0r} \cos \theta_r = E_{0t} \cos \theta_t. \quad (4.36)$$

In much the same way as before, continuity of the tangential components of \mathbf{B}/μ yields

$$\frac{1}{\mu_i v_i} E_{0i} + \frac{1}{\mu_r v_r} E_{0r} = \frac{1}{\mu_t v_t} E_{0t}. \quad (4.37)$$

Using the fact that $\mu_i = \mu_r$ and $\theta_i = \theta_r$, we can combine these formulas to obtain two more of the *Fresnel equations*:

$$r_{\parallel} \equiv \left(\frac{E_{0r}}{E_{0i}} \right)_{\parallel} = \frac{\frac{n_t}{\mu_t} \cos \theta_t - \frac{n_i}{\mu_i} \cos \theta_i}{\frac{n_t}{\mu_t} \cos \theta_t + \frac{n_i}{\mu_i} \cos \theta_i} \quad (4.38)$$

and

$$t_{\parallel} \equiv \left(\frac{E_{0t}}{E_{0i}} \right)_{\parallel} = \frac{2 \frac{n_i}{\mu_i} \cos \theta_i}{\frac{n_i}{\mu_i} \cos \theta_i + \frac{n_t}{\mu_t} \cos \theta_t}. \quad (4.39)$$

When both media forming the interface are dielectrics, the amplitude coefficients become

$$r_{\parallel} = \frac{n_t \cos \theta_i - n_i \cos \theta_t}{n_i \cos \theta_i + n_t \cos \theta_t} \quad (4.40)$$

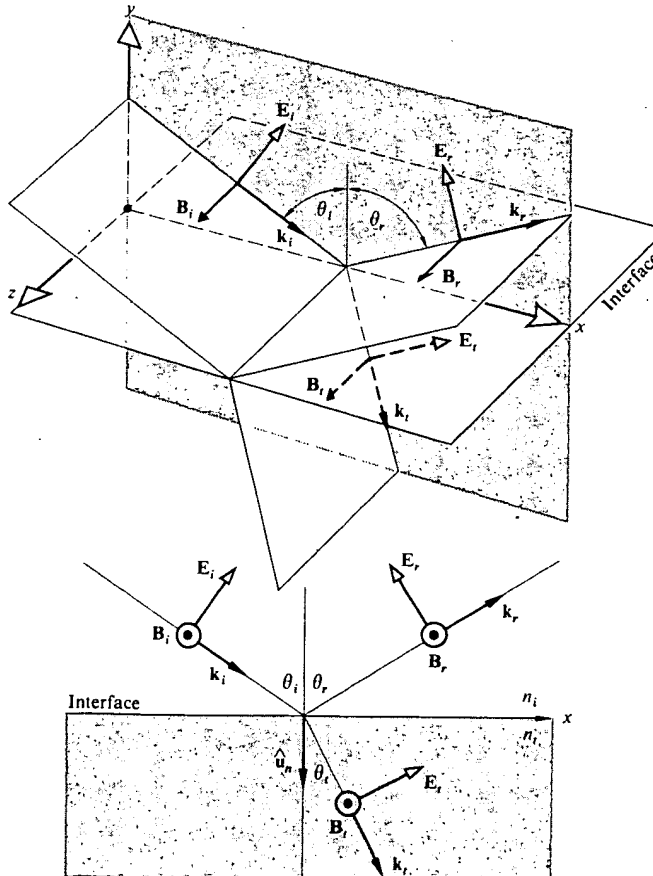


Figure 4.21 An incoming wave whose \mathbf{E} -field is in the plane of incidence.

and

$$t_{\parallel} = \frac{2 n_i \cos \theta_i}{n_i \cos \theta_i + n_t \cos \theta_t}. \quad (4.41)$$

One further notational simplification can be made by availing ourselves of Snell's law, whereupon the Fresnel equations for dielectric media become (Problem 4.23)

$$r_{\perp} = - \frac{\sin (\theta_i - \theta_t)}{\sin (\theta_i + \theta_t)} \quad (4.42)$$

$$r_{\parallel} = + \frac{\tan (\theta_i - \theta_t)}{\tan (\theta_i + \theta_t)} \quad (4.43)$$

$$t_{\perp} = + \frac{2 \sin \theta_t \cos \theta_i}{\sin (\theta_i + \theta_t)} \quad (4.44)$$

$$t_{\parallel} = + \frac{2 \sin \theta_t \cos \theta_i}{\sin (\theta_i + \theta_t) \cos (\theta_i - \theta_t)}. \quad (4.45)$$

A note of caution must be introduced before we move on to examine the considerable significance of the preceding calculation. Bear in mind that the directions (or more precisely, the phases) of the fields in Figs. 4.20 and 4.21 were selected rather arbitrarily. For example, in Fig. 4.20 we could have assumed that \mathbf{E}_i pointed inward, whereupon \mathbf{B}_i would have had to be reversed as well. Had we done that, the sign of r_{\perp} would have turned out to be positive, leaving the other amplitude coefficients unchanged. The signs appearing in Eqs. (4.42) through (4.45), in this case positive, except for the first, correspond to the particular set of field directions selected. The minus sign, as we will see, just means that we didn't guess correctly concerning \mathbf{E}_i in Fig. 4.20. Nonetheless, be aware that the literature is not standardized, and all possible sign variations have been labeled *Fresnel equations*—to avoid confusion *they must be related to the specific field directions from which they were derived*.

4.3.3 Interpretation of the Fresnel Equations

This section is devoted to an examination of the physical implications of the Fresnel equations. In particular we are interested in determining the fractional amplitudes and flux densities that are reflected and refracted. In

addition we shall be concerned with any possible phase shifts that might be incurred in the process.

i) Amplitude Coefficients

Let's briefly examine the form of the amplitude coefficients over the entire range of θ_i values. At nearly normal incidence ($\theta_i \approx 0$) the tangents in Eq. (4.43) are essentially equal to sines, in which case

$$[r_{\parallel}]_{\theta_i=0} = [-r_{\perp}]_{\theta_i=0} = \left[\frac{\sin(\theta_i - \theta_t)}{\sin(\theta_i + \theta_t)} \right]_{\theta_i=0}.$$

We will come back to the physical significance of the minus sign presently. After we have expanded the sines and used Snell's law, this expression becomes

$$[r_{\parallel}]_{\theta_i=0} = [-r_{\perp}]_{\theta_i=0} = \left[\frac{n_t \cos \theta_i - n_i \cos \theta_t}{n_t \cos \theta_i + n_i \cos \theta_t} \right]_{\theta_i=0}, \quad (4.46)$$

which follows as well from Eqs. (4.34) and (4.40). In the limit, as θ_i goes to 0, $\cos \theta_i$ and $\cos \theta_t$ both approach one, and consequently

$$[r_{\parallel}]_{\theta_i=0} = [-r_{\perp}]_{\theta_i=0} = \frac{n_t - n_i}{n_t + n_i}. \quad (4.47)$$

Thus, for example, at an air ($n_i = 1$) glass ($n_t = 1.5$) interface at nearly normal incidence, the reflection coefficients equal ± 0.2 .

When $n_t > n_i$ it follows from Snell's law that $\theta_i > \theta_t$, and r_{\perp} is negative for all values of θ_i (Fig. 4.22). In contrast, r_{\parallel} starts out positive at $\theta_i = 0$ and decreases gradually until it equals zero when $(\theta_i + \theta_t) = 90^\circ$, since $\tan \pi/2$ is infinite. The particular value of the incident angle for which this occurs is denoted by θ_p and is referred to as the **polarization angle** (see Section 8.6.1). As θ_i increases beyond θ_p , r_{\parallel} becomes progressively more negative, reaching -1.0 at 90° . If you place a single sheet of glass, a microscope slide, on this page and look straight down into it ($\theta_i = 0$), the region beneath the glass will seem decidedly grayer than the rest of the paper, because the slide will reflect at both its interfaces, and the light reaching and returning from the paper will be diminished appreciably. Now hold the slide near your eye and again view the page through it as you tilt it, increasing θ_i . The amount of light reflected will increase, and it will become more difficult to see

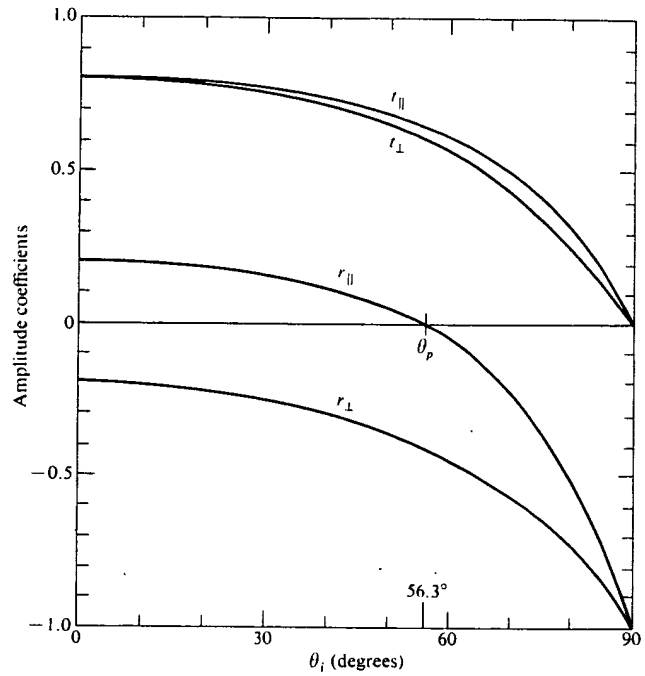


Figure 4.22 The amplitude coefficients of reflection and transmission as a function of incident angle. These correspond to external reflection $n_t > n_i$ at an air-glass interface ($n_{ii} = 1.5$).

the page through the glass. When $\theta_i \approx 90^\circ$ the slide will look like a perfect mirror as the reflection coefficients (Fig. 4.22) go to -1.0 . Even a rather poor surface, such as the cover of this book, will be mirrorlike at glancing incidence. Hold the book horizontally at the level of the middle of your eye and face a bright light; you will see the source reflected rather nicely in the cover. This suggests that even x-rays could be mirror-reflected at glancing incidence (p. 210), and modern x-ray telescopes are based on that very fact.

At normal incidence Eqs. (4.35) and (4.41) lead rather straightforwardly to

$$[t_{\parallel}]_{\theta_i=0} = [t_{\perp}]_{\theta_i=0} = \frac{2n_i}{n_i + n_t}. \quad (4.48)$$

It will be shown in Problem 4.24 that the expression

$$t_{\perp} + (-r_{\perp}) = 1 \quad (4.49)$$

holds for all θ_i , whereas

$$t_{\parallel} + r_{\parallel} = 1 \quad (4.50)$$

is true only at normal incidence.

The foregoing discussion, for the most part, was restricted to the case of **external reflection** (i.e., $n_t > n_i$). The opposite situation of **internal reflection**, in which the incident medium is the more dense ($n_i > n_t$), is of interest as well. In that instance $\theta_t > \theta_i$, and r_{\perp} , as described by Eq. (4.42), will always be positive. Figure 4.23 shows that r_{\perp} increases from its initial value (4.47) at $\theta_i = 0$, reaching +1 at what is called the **critical angle**, θ_c . Specifically, θ_c is the special value of the incident angle for which $\theta_t = \pi/2$. Likewise, r_{\parallel} starts off negatively (4.47) at $\theta_i = 0$ and thereafter increases, reaching +1 at $\theta_i = \theta_c$, as is evident from the Fresnel equation (4.40). Again, r_{\parallel} passes through zero at the *polarization angle* θ'_p . It is left for Problem 4.34 to show that the polarization angles θ'_p and θ_p for internal and external reflection at the interface between the same media are simply the complements of each other. We will return to internal reflection in Section 4.3.4, where it will be shown that r_{\perp} and r_{\parallel} are complex quantities for $\theta_i > \theta_c$.

ii) Phase Shifts

It should be evident from Eq. (4.42) that r_{\perp} is negative regardless of θ_i when $n_t > n_i$. Yet we saw earlier that had we chosen $[\mathbf{E}_r]_{\perp}$ in Fig. 4.20 to be in the opposite direction, the first Fresnel equation (4.42) would have changed signs, causing r_{\perp} to become a positive quantity. Thus the sign of r_{\perp} is associated with the relative directions of $[\mathbf{E}_{0i}]_{\perp}$ and $[\mathbf{E}_{0r}]_{\perp}$. Bear in mind that a reversal of $[\mathbf{E}_{0r}]_{\perp}$ is tantamount to introducing a phase shift, $\Delta\varphi_{\perp}$, of π radians into $[\mathbf{E}_r]_{\perp}$. Hence at the boundary $[\mathbf{E}_i]_{\perp}$ and $[\mathbf{E}_r]_{\perp}$ will be antiparallel and therefore π out of phase with each other, as indicated by the negative value of r_{\perp} . When we consider components normal to the plane of incidence, there is no confusion as to whether two fields are in phase or π radians out of phase: if parallel, they're in phase; if antiparallel, they're π out of phase. In summary, then, *the component of the electric field normal to the plane of incidence undergoes a phase shift of π radians upon reflection when the incident medium has a lower index than the transmitting medium.*

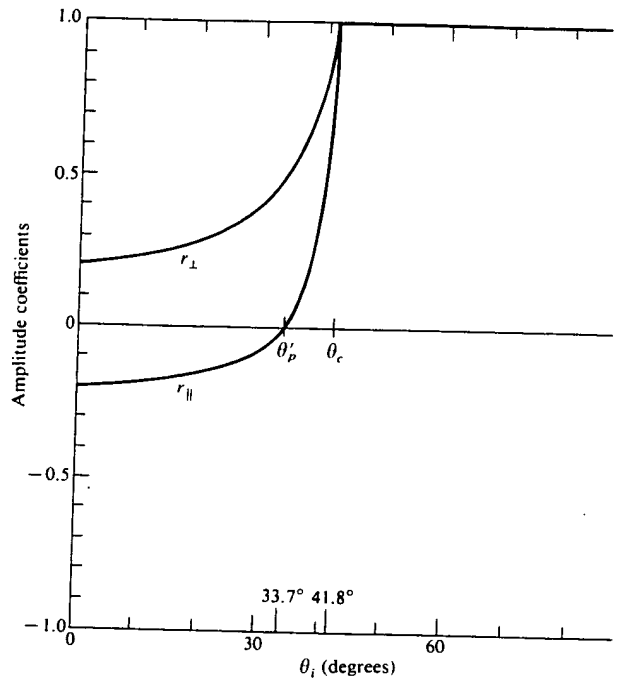


Figure 4.23 The amplitude coefficients of reflection as a function of incident angle. These correspond to internal reflection $n_t < n_i$ at an air-glass interface ($n_{ti} = 1/1.5$).

Similarly, t_{\perp} and t_{\parallel} are always positive and $\Delta\varphi = \pi$. Furthermore, when $n_i > n_t$ no phase shift in the normal component results on reflection, that is, $\Delta\varphi_{\perp} = 0$ so long as $\theta_i < \theta_c$.

Things are a bit less obvious when we deal with $[\mathbf{E}_i]$, $[\mathbf{E}_r]_{\parallel}$, and $[\mathbf{E}_r]_{\perp}$. It now becomes necessary to define more explicitly what is meant by *in phase*, since the field vectors are coplanar but generally not colinear. The field directions were chosen in Figs. 4.20 and 4.21 such that if you looked down any one of the propagating vectors toward the direction from which the light was coming, \mathbf{E} , \mathbf{B} , and \mathbf{k} would appear to have the same relative orientation whether the ray was incident, reflected, or transmitted. We can use this as the required condition for two \mathbf{E} -fields to be in phase. Equivalently, but more simply, *two fields in the incident plane are in phase if their y-components are parallel and are out of phase if their y-components are antiparallel*.

if the components are antiparallel. Notice that when two \mathbf{E} -fields are out of phase so too are their associated \mathbf{B} -fields and vice versa. With this definition we need only look at the vectors normal to the plane of incidence, whether they be \mathbf{E} or \mathbf{B} , to determine the relative phase of the accompanying fields in the incident plane. Thus in Fig. 4.24(a) \mathbf{E}_i and \mathbf{E}_r are in phase, as are \mathbf{B}_i and \mathbf{B}_r , whereas \mathbf{E}_i and \mathbf{E}_t are out of phase, along with \mathbf{B}_i and \mathbf{B}_t . Similarly, in Fig. 4.24(b) \mathbf{E}_i , \mathbf{E}_r , and \mathbf{E}_t are in phase, as are \mathbf{B}_i , \mathbf{B}_r , and \mathbf{B}_t .

Now, the amplitude reflection coefficient for the parallel component is given by

$$r_{\parallel} = \frac{n_i \cos \theta_i - n_r \cos \theta_r}{n_i \cos \theta_i + n_r \cos \theta_r},$$

which is positive ($\Delta\phi_{\parallel} = 0$) as long as

$$n_i \cos \theta_i - n_r \cos \theta_r > 0,$$

that is, if

$$\sin \theta_i \cos \theta_i - \cos \theta_r \sin \theta_r > 0$$

or equivalently

$$\sin(\theta_i - \theta_r) \cos(\theta_i + \theta_r) > 0. \quad (4.51)$$

This will be the case for $n_i < n_r$ if

$$(\theta_i + \theta_r) < \pi/2. \quad (4.52)$$

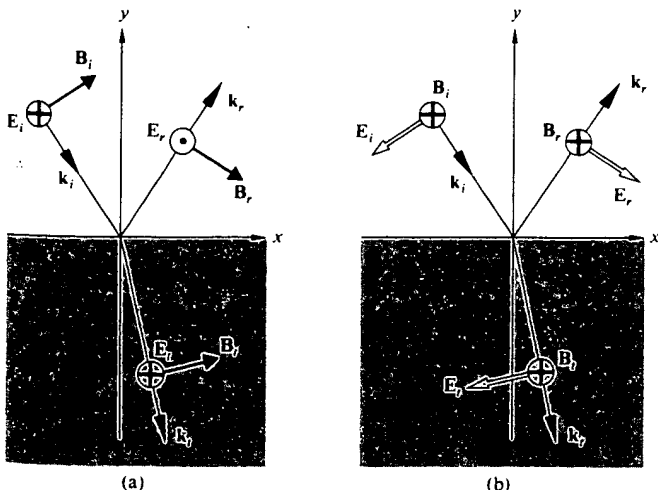


Figure 4.24 Field orientations and phase shifts.

and for $n_i > n_r$ when

$$(\theta_i + \theta_r) > \pi/2. \quad (4.53)$$

Thus when $n_i < n_r$, $[\mathbf{E}_{0r}]_{\parallel}$ and $[\mathbf{E}_{0i}]_{\parallel}$ will be in phase ($\Delta\phi_{\parallel} = 0$) until $\theta_i = \theta_p$ and out of phase by π radians thereafter. The transition is not actually discontinuous, since $[\mathbf{E}_{0r}]_{\parallel}$ goes to zero at θ_p . In contrast, for internal reflection r_{\parallel} is negative until θ'_p , which means that $\Delta\phi_{\parallel} = \pi$. From θ'_p to θ_c , r_{\parallel} is positive and $\Delta\phi_{\parallel} = 0$. Beyond θ_c , r_{\parallel} becomes complex, and $\Delta\phi_{\parallel}$ gradually increases to π at $\theta_i = 90^\circ$.

Figure 4.25, which summarizes these conclusions, will be of continued use to us. The actual functional form of $\Delta\phi_{\parallel}$ and $\Delta\phi_{\perp}$ for internal reflection in the region where $\theta_i > \theta_c$ can be found in the literature,* but the curves depicted here will suffice for our purposes. Figure 4.25(e) is a plot of the relative phase shift between the parallel and perpendicular components, that is, $\Delta\phi_{\parallel} - \Delta\phi_{\perp}$. It is included here because it will be useful later on (e.g., when we consider polarization effects). Finally, many of the essential features of this discussion are illustrated in Figs. 4.26 and 4.27. The amplitudes of the reflected vectors are in accord with those of Figs. 4.22 and 4.23 (for an air-glass interface), and the phase shifts agree with those of Fig. 4.25.

Many of these conclusions can be verified with the simplest experimental equipment, namely, two linear polarizers, a piece of glass, and a small source, such as a flashlight or high-intensity lamp. By placing one polarizer in front of the source (at 45° to the plane of incidence), you can easily duplicate the conditions of Fig. 4.26. For example, when $\theta_i = \theta_p$ [Fig. 4.26(b)] no light will pass through the second polarizer if its transmission axis is parallel to the plane of incidence. In comparison, at near-glancing incidence the reflected beam will vanish when the axes of the two polarizers are almost normal to each other.

iii) Reflectance and Transmittance

Consider a circular beam of light incident on a surface, as shown in Fig. 4.28, such that there is an illuminated spot of area A . Recall that the power per unit area

* Born and Wolf, *Principles of Optics*, p. 49.

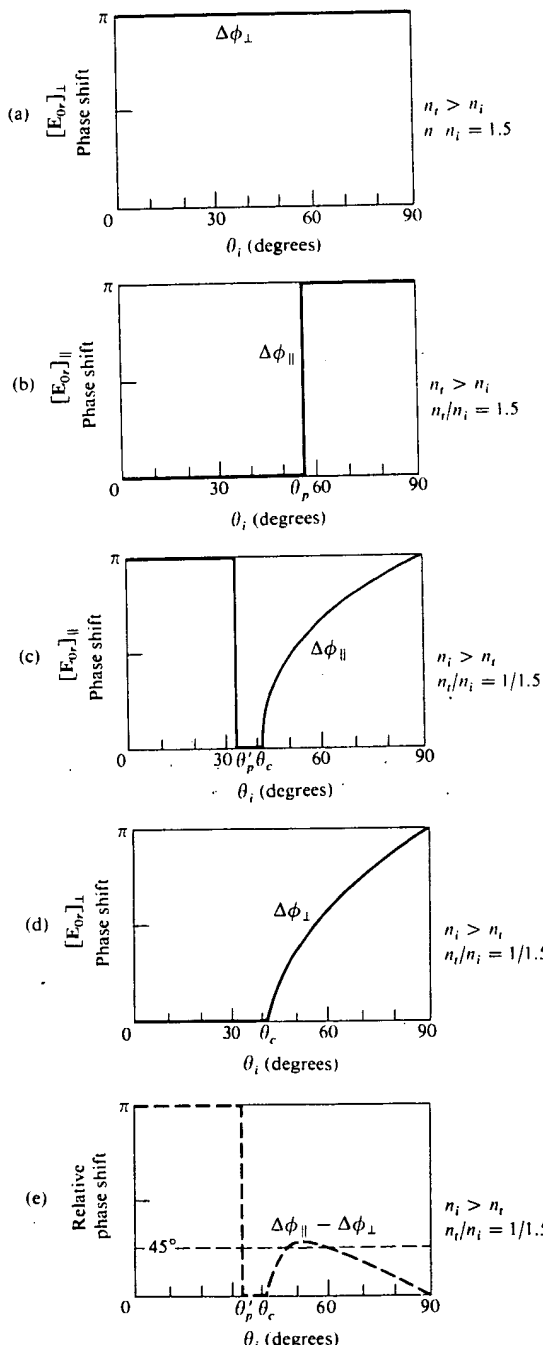


Figure 4.25 Phase shifts for the parallel and perpendicular components of the \mathbf{E} -field corresponding to internal and external reflection.

crossing a surface in vacuum whose normal is parallel to \mathbf{S} , the Poynting vector, is given by

$$\mathbf{S} = c^2 \epsilon_0 \mathbf{E} \times \mathbf{B}. \quad [3.48]$$

Furthermore, the radiant flux density (W/m^2) or irradiance is

$$I = \langle S \rangle = \frac{c\epsilon_0}{2} E_0^2. \quad [3.52]$$

This is the average energy per unit time crossing a unit area normal to \mathbf{S} (in isotropic media \mathbf{S} is parallel to \mathbf{k}). In the case at hand (Fig. 4.28), let I_i , I_r , and I_t be the incident, reflected, and transmitted flux densities, respectively. The cross-sectional areas of the incident, reflected, and transmitted beams are, respectively, $A \cos \theta_i$, $A \cos \theta_r$, and $A \cos \theta_t$. Accordingly, the incident power is $I_i A \cos \theta_i$; this is the energy per unit time flowing in the incident beam and it's therefore the power arriving on the surface over A . Similarly, $I_r A \cos \theta_r$ is the power in the reflected beam, and $I_t A \cos \theta_t$ is the power being transmitted through A . We define the **reflectance** R to be the ratio of the reflected power (or flux) to the incident power:

$$R \equiv \frac{I_r \cos \theta_r}{I_i \cos \theta_i} = \frac{I_r}{I_i}. \quad (4.54)$$

In the same way, the **transmittance** T is defined as the ratio of the transmitted to the incident flux and is given by

$$T \equiv \frac{I_t \cos \theta_t}{I_i \cos \theta_i}. \quad (4.55)$$

The quotient I_r/I_i equals $(v_r \epsilon_r E_{0r}^2/2)/(v_i \epsilon_i E_{0i}^2/2)$, and since the incident and reflected waves are in the same medium, $v_r = v_i$, $\epsilon_r = \epsilon_i$, and

$$R = \left(\frac{E_{0r}}{E_{0i}} \right)^2 = r^2. \quad (4.56)$$

In like fashion (assuming $\mu_i = \mu_t = \mu_0$),

$$T = \frac{n_t \cos \theta_t}{n_i \cos \theta_i} \left(\frac{E_{0i}}{E_{0i}} \right)^2 = \left(\frac{n_t \cos \theta_t}{n_i \cos \theta_i} \right) t^2, \quad (4.57)$$

where use was made of the fact that $\mu_0 \epsilon_i = 1/v_i^2$ and $\mu_0 v_i \epsilon_i = n_i/c$. Notice that at normal incidence, which is a situation of great practical interest, $\theta_t = \theta_i = 0$, and

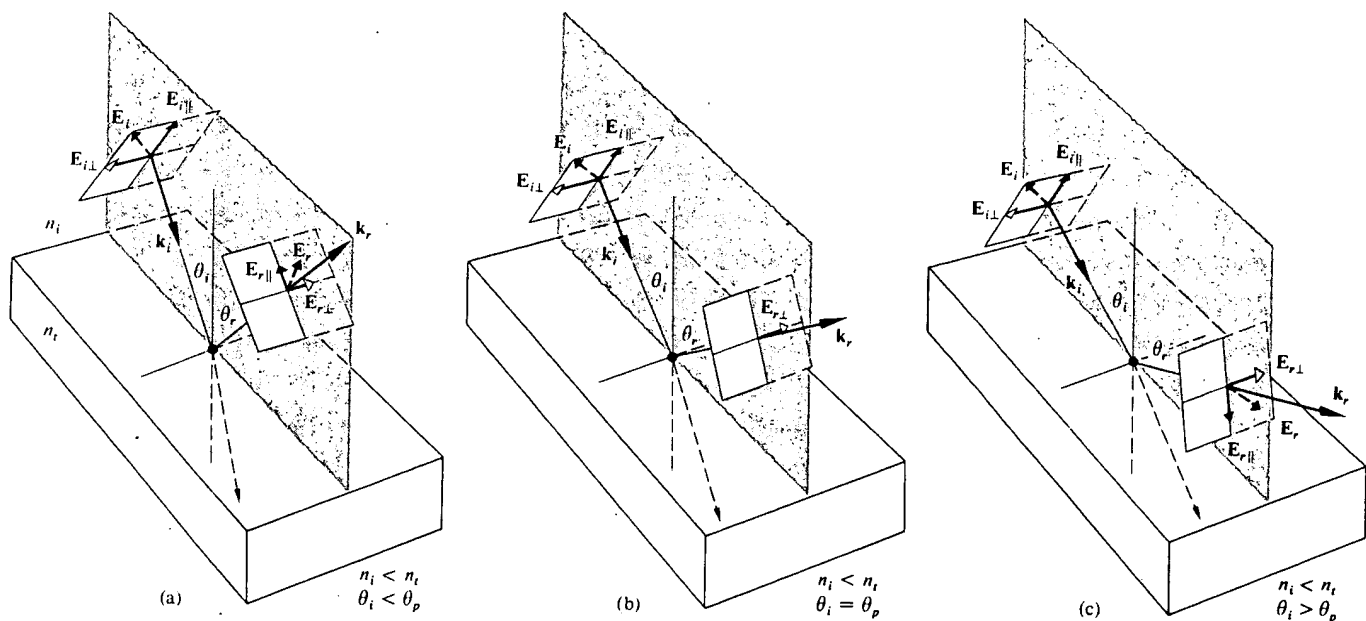


Figure 4.26 The reflected E-field at various angles concomitant with external reflection.

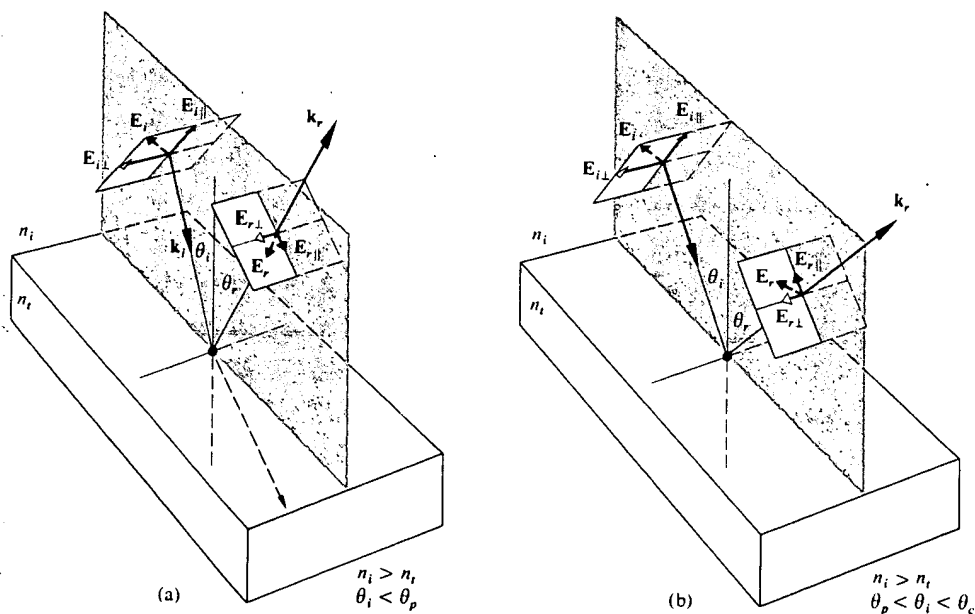


Figure 4.27 The reflected E-field at various angles concomitant with internal reflection.

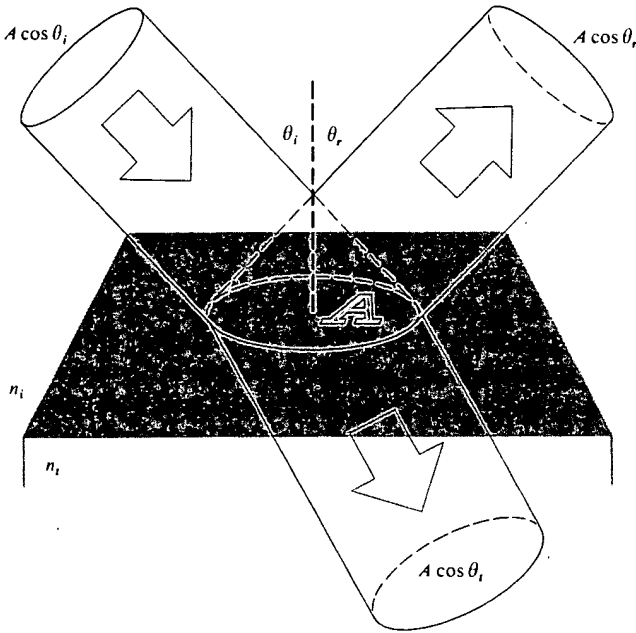


Figure 4.28 Reflection and transmission of an incident beam.

the transmittance [Eq. (4.55)], like the reflectance [Eq. (4.54)], is then simply the ratio of the appropriate irradiances. Since $R = r^2$, we need not worry about the sign of r in any particular formulation, and that makes reflectance a convenient notion. Observe that in Eq. (4.57) T is not simply equal to t^2 , for two reasons. First, the ratio of the indices of refraction must be there, since the speeds at which energy is transported into and out of the interface are different, in other words, $I \propto v$, from Eq. (3.47). Second, the cross-sectional areas of the incident and reflected beams are different, and so the energy flow per unit area is affected accordingly, and that manifests itself in the presence of the ratio of the cosine terms.

Let's now write an expression representing the conservation of energy for the configuration depicted in Fig. 4.26. In other words, the total energy flowing into area A per unit time must equal the energy flowing outward from it per unit time:

$$I_i A \cos \theta_i = I_r A \cos \theta_r + I_t A \cos \theta_t. \quad (4.58)$$

When both sides are multiplied by c this expression

becomes

$$n_i E_{0i}^2 \cos \theta_i = n_i E_{0r}^2 \cos \theta_r + n_t E_{0t}^2 \cos \theta_t$$

or

$$1 = \left(\frac{E_{0r}}{E_{0i}} \right)^2 + \left(\frac{n_t \cos \theta_t}{n_i \cos \theta_i} \right) \left(\frac{E_{0t}}{E_{0i}} \right)^2. \quad (4.59)$$

But this is simply

$$R + T = 1, \quad (4.60)$$

where there was no absorption. It is convenient to use the component forms, that is,

$$R_{\perp} = r_{\perp}^2 \quad (4.61)$$

$$R_{\parallel} = r_{\parallel}^2 \quad (4.62)$$

$$T_{\perp} = \left(\frac{n_t \cos \theta_t}{n_i \cos \theta_i} \right) t_{\perp}^2 \quad (4.63)$$

and

$$T_{\parallel} = \left(\frac{n_t \cos \theta_t}{n_i \cos \theta_i} \right) t_{\parallel}^2, \quad (4.64)$$

which are illustrated in Fig. 4.29. Furthermore, it can be shown (Problem 4.39) that

$$R_{\parallel} + T_{\parallel} = 1 \quad (4.65)$$

and

$$R_{\perp} + T_{\perp} = 1. \quad (4.66)$$

When $\theta_i = 0$ the incident plane becomes undefined, and any distinction between the parallel and perpendicular components of R and T vanishes. In this case Eqs. (4.61) through (4.64), along with (4.47) and (4.48), lead to

$$R = R_{\parallel} = R_{\perp} = \left(\frac{n_t - n_i}{n_t + n_i} \right)^2 \quad (4.67)$$

and

$$T = T_{\parallel} = T_{\perp} = \frac{4n_t n_i}{(n_t + n_i)^2}. \quad (4.68)$$

Thus 4% of the light incident normally on an air-glass interface will be reflected back, whether internally, $n_i > n_t$, or externally, $n_i < n_t$ (Problem 4.40). This will

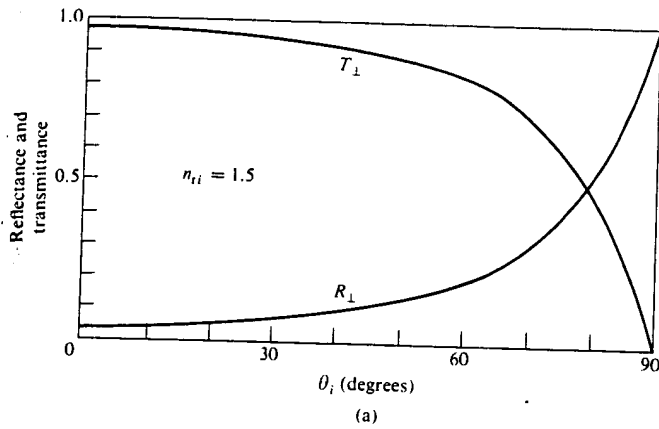


Figure 4.29 Reflectance and transmittance versus incident angle.

obviously be of great concern to anyone who is working with a complicated lens system, which might have 10 or 20 such air-glass boundaries. Indeed, if you look perpendicularly into a stack of about 50 microscope slides (cover-glass slides are much thinner and easier to handle in large quantities), most of the light will be reflected. The stack will look very much like a mirror

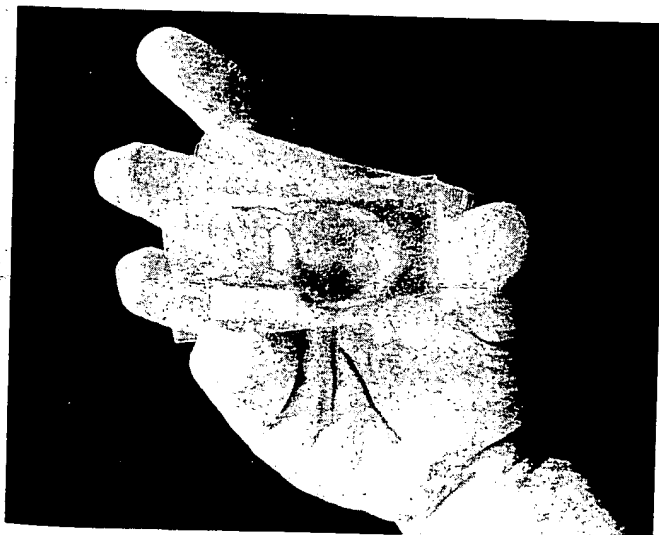
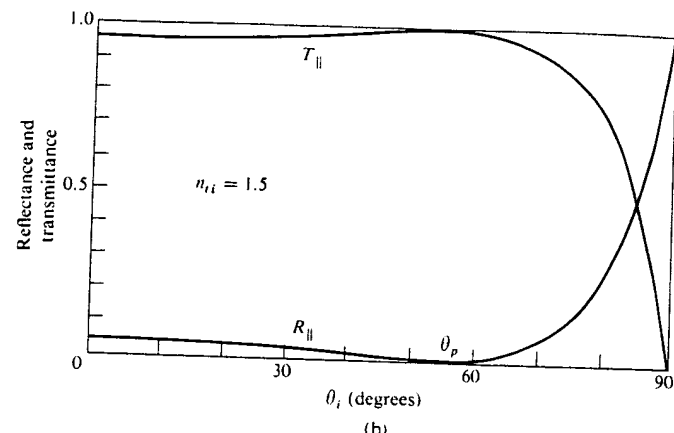


Figure 4.30 Near normal reflection off a stack of microscope slides. You can see the image of the camera that took the picture. (Photo by E.H.)

(Fig. 4.30). Figure 4.31 is a plot of the reflectance at a single interface, assuming normal incidence for various transmitting media in air. Figure 4.32 depicts the corresponding dependence of the transmittance at normal incidence on the number of interfaces and the index of the medium. Of course, this is why you can't see through a roll of "clear" smooth-surfaced plastic tape,

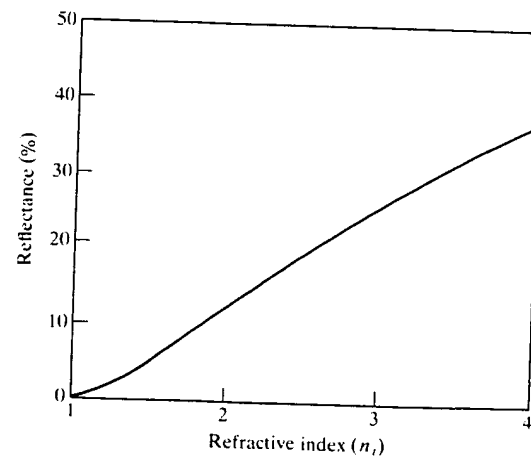


Figure 4.31 Reflectance at normal incidence in air ($n_i = 1.0$) at a single interface.

SPIE Milestone Series

Volume MS 34

Selected Papers on

Holographic and Diffractive Lenses and Mirrors

Thomas W. Stone and Brian J. Thompson, *Editors*

*The Institute of Optics
University of Rochester*

Brian J. Thompson
General Editor, SPIE Milestone Series



S P I E O P T I C A L E N G I N E E R I N G P R E S S

A Publication of SPIE—The International Society for Optical Engineering
Bellingham, Washington USA

Holographic mirrors

José R. Magariños

Daniel J. Coleman

Farrand Optical Company, Inc.
117 Wall Street
Valhalla, New York 10595

Abstract. Reflection holograms of the volume-phase type fabricated with dichromated gelatin have the advantages of achieving efficiencies very close to 100%, very low noise, and, due to their wavelength selectivity, a chromatic dispersion that can be acceptable in many applications. For several years, the production of these holograms has been investigated with the goal of controlling their processing and achieving high quality and good repeatability. Holographic spherical mirrors with dimensions larger than 82 cm were used in the holographic Pancake Window optical simulator suitable for the training of pilots. These holographic spherical mirrors were also built as compound holograms providing a "white" spectral response very similar to that of conventional mirrors. Prototypes of holographic combiners were fabricated and analyzed. Holographic mirrors were also manufactured for use as notch filters, which selectively reflect very narrow spectral frequencies, for example, laser radiation. They offer the advantages of high optical densities with large field-of-view coverage and high photopic transmission.

Subject terms: holography; holographic mirror; dichromated gelatin; holographic optical element; optical simulator; holographic combiner; holographic notch filter.

Optical Engineering 24(5), 769-780 (September/October 1985).

CONTENTS

1. Introduction
2. Holographic mirrors
 - 2.1. Diffraction processes
 - 2.2. Photographic process
 - 2.3. Interference process and construction geometries
 - 2.4. Properties
3. Technology
 - 3.1. Materials
 - 3.1.1. Gelatin film
 - 3.2. New dichromated gelatin process theory
 4. Holographic mirror characteristics
 - 4.1. Diffraction efficiency
 - 4.2. Spectral response
 - 4.3. Spectral bandwidth
 - 4.4. Optical properties
 - 4.5. Endurance of the holographic mirrors
 5. Facilities
 6. Applications
 - 6.1. Holographic Pancake Window
 - 6.2. Holographic notch filters
 - 6.3. Holographic combiners
 7. Conclusions
 8. References

1. INTRODUCTION

Holographic mirrors are optical elements that diffract light as conventional mirrors reflect light. These holographic mirrors behave according to the laws of diffraction instead of reflection and consequently have specific differences that open new fields of applications but also require a new technology. Generally, holographic mirrors are not substitutes for conventional mirrors. In particular applications they offer significant advantages or can be used in optical con-

figurations that are not achievable using conventional mirrors.

Holographic optical elements (HOEs) or diffractive optics are common designations for a type of hologram that, because of its property of focusing light, is analogous to conventional optical elements. Transmission-type holograms relate to lenses, and reflection-type holograms (holographic mirrors) relate to mirrors. These holograms, besides being classified as transmission or reflection, are also classified as thin or volume and as absorption or phase. Holograms can perform quite differently depending on their type.

The most striking characteristics of holograms as optical elements are that they strongly disperse light (usually a serious disadvantage) and that their optical configuration is independent of their substrate geometry (a holographic spherical mirror, for example, recorded in an emulsion on a flat substrate will focus light in spite of its flat physical configuration). The disadvantage of high dispersion can be avoided using monochromatic sources or can be reduced, as in the case of holographic mirrors, since they can work simultaneously as monochromatic filters. Because of their independence from their substrates, they have found unique applications as holographic beam-splitter mirrors in head-up systems, in holographic notch filters, and in specific optical systems like the Pancake Window optical simulator.

Not only is the performance of holographic mirrors evaluated with respect to their optical aberrations, but strong consideration is given to their diffraction efficiency and low noise. For most applications, diffraction efficiencies larger than 50% and in some cases closer to 100% are required. High signal-to-noise ratios are usually needed. These requirements narrow the choice of hologram to the volume-phase type and the material, especially for holographic mirrors, to a dichromated gelatin film.

The dichromated gelatin film is basically a photoresist film which has its solubility in water changed by exposure to light. In the photographic process the film is hard enough to be insoluble in water but still soft enough so exposure to light can be registered as a variation in hardness or index of refraction. The diffraction efficiency achieved with this film is practically 100%. The repeatability and merit of this process has been controversial, but recently, with process controls and proper facilities, excellent results have been

Invited Paper HO-109 received April 17, 1985; revised manuscript received May 28, 1985; accepted for publication May 31, 1985; received by Managing Editor June 21, 1985. This paper is a revision of Paper 523-31 which was presented at the SPIE conference on Applications of Holography, Jan. 21-23, 1985, Los Angeles, Calif. The paper presented there appears (unreferred) in SPIE Proceedings Vol. 523. ©1985 Society of Photo-Optical Instrumentation Engineers.

achieved.

Holographic mirrors of the volume-phase type^{1,2} are governed by Bragg's law of diffraction. Its efficiency and angular and spectral sensitivity are predicted by the coupled-wave or modal theory.³ A very successful approximate theory, the two-wave coupled-wave theory, also known as the Kogelnik theory,⁴ is commonly used to calculate the performance of these holograms.

This paper will describe the physical and optical characteristics of holographic mirrors, their production using the dichromated gelatin holographic process, and the applications developed at Farrand Optical Company.

2. HOLOGRAPHIC MIRRORS

Holographic mirrors are volume-phase reflection-type holograms. The reflection is not a physical reflection effect, but light is diffracted by them in the same medium of incidence. A thick- or volume-type hologram is the recording of an interferogram throughout the entire volume of the recording film (three-dimensional recording) and not just over the surface (two-dimensional recording). Phase-type holograms are free of absorption, and the transmittance function is modulated in its permittivity (index of refraction). The theoretical diffraction efficiency of a volume-phase hologram can be 100%.

The holographic process embraces photochemical, interference, and diffractive phenomena. The photochemical phenomenon is the recording of the hologram and is studied empirically, evaluating the results of using different materials and sensitizers. A formal theory is not yet available for the particular process that will be referred to here. The formation of the recorded interferogram is an interference phenomenon that can be analytically described, and straightforward solutions are easily obtainable. Extracting the information contained in the hologram or defining its optical characteristics requires solving a diffraction problem whose solution is generally unknown or very complicated. Only in a few simple cases are analytical solutions obtainable. Together these three phenomena define the holographic mirrors.

2.1. Diffraction processes

Holographic mirrors of the volume-phase type are treated as a particular case of a generalized three-dimensional diffraction grating. Rigorous grating diffraction theories have been formulated, and the two best known are the coupled-wave theory, which uses an expansion in terms of the space harmonics of the fields in the periodic structure, and the modal theory, which uses an expansion in terms of the allowable modes of the periodic medium or waveguide modes in the grating region. These exact formulations are simplified with approximate theories in which higher order waves, boundary effects, etc., are neglected. The best known of the approximate theories is due to Kogelnik, a two-wave first-order coupled-wave theory. In this theory the higher-order waves and the second derivatives of field amplitude are neglected, providing analytical solutions for many practical cases, covering (a) phase, absorption, and mixed gratings; (b) on-Bragg and off-Bragg incidence; (c) unslanted and slanted gratings; and (d) polarization of the waves.

The coupled-wave theory predicts that the efficiency of a volume-phase reflection hologram can reach a value of 100% and is defined as

$$\eta = \frac{1}{1 + \frac{1 - (\xi^2/\nu^2)}{\sinh^2(\nu^2 - \xi^2)^{1/2}}}, \quad (1)$$

where $\xi = 2\pi n_0 T \Delta \lambda / \lambda^2$ and $\nu = \pi T n_1 / \lambda$ are functions of the wavelength response in air, λ , the average index of refraction of the hologram, n_0 , and its thickness T , the index modulation n_1 , and the spectral sensitivity $\Delta \lambda$.

The Bragg law of diffraction is a relation between the spacing of the planes of diffraction, d , the wavelength of the light, λ , and the semiangle θ between the incident and the diffracted ray. The law is expressed analytically by $2dn_0 \sin \theta = m\lambda$, where m is an integer. This law can be differentiated to establish an interdependence between the angular selectivity and the spectral selectivity, or the effect of an incremental deviation from the Bragg conditions. The spectral selectivity of holographic mirrors can be very high, thus making them capable of performing as narrowband spectral filters. Their angular sensitivity is quite low, and relatively large field-of-view angles can be achieved.

2.2. Photographic process

The photographic material presently used in the production of these holographic mirrors is a gelatin film. It is sensitized with a solution of ammonium dichromate, and when exposed to light it behaves as a photoresist: the molecular chains in the regions of the film exposed to more light have more crosslinking, and so the physical characteristics of the film are slightly changed. Specifically, these regions swell less when immersed in water, and, if rapidly dehydrated, differential strains are produced between regions of maximum and minimum swelling. These strains modify the index of refraction. Consequently, surfaces of interference with a maximum of light intensity correspond with surfaces of maximum crosslinking, minimum swelling, and minimum variation of the index of refraction. The opposite will be the case for the surfaces of interference where light intensity is a minimum. Planes of diffraction are then defined by this modulation of the index of refraction.

From the study of all the available materials for the production of holographic mirrors,⁵ dichromated gelatin is the closest to the ideal material: the achievable efficiencies are practically the theoretical limit (100%), the spatial resolution is dimensionally molecular, the scattering is minimal, the absorption is negligible, and the hologram has good resistance to radiation and to changes in temperature. The gelatin has disadvantages: principally, a low photochemical sensitivity restricted to the blue-green spectral region and an intolerance to moisture. In dealing with this material Farrand Optical Company and other groups have demonstrated results that are controllable and reproducible.

2.3. Interference process and construction geometries

A volume-phase reflection hologram is produced by the interference of two coherent and monochromatic waves that are incident in opposite directions in a photosensitive film. The interference forms standing waves or surfaces of interference where the intensity of light is a maximum or a minimum. After the interferogram is registered, these surfaces become surfaces of diffraction and the holographic mirror is considered a three-dimensional grating in which light is diffracted, obeying Bragg's law.

A direct analogy can be established between holographic mirrors and conventional mirrors. This analogy is obvious when the foci of a conventional mirror are correlated with the construction geometry of the hologram or the relative position of the point sources that are the origin (of convergence or divergence) of the two interfering waves. Figure 1 shows this correspondence. In this two-dimensional representation the foci of a conic (parabola, ellipse, hyperbola, or circumference) define the position of the point sources that will produce a parabolic, ellipsoidal, hyperbolic, or spherical holographic mirror. A holographic spherical, aspheric, or any other configuration mirror can be made by changing the relative position of the illumination point sources in the construction geometry: for a plane mirror the construction points are at infinity, for a spherical mirror both are at the center of curvature, for ellipsoidal mirrors they are at the foci of the correspondent ellipsoid, etc. Cylindrical and other configuration holographic mirrors can be made by optically modifying the wavefronts. In all these cases, only a photographic setup is required and no material grinding, polishing, etc., are needed, as are required in conventional mirror construction.

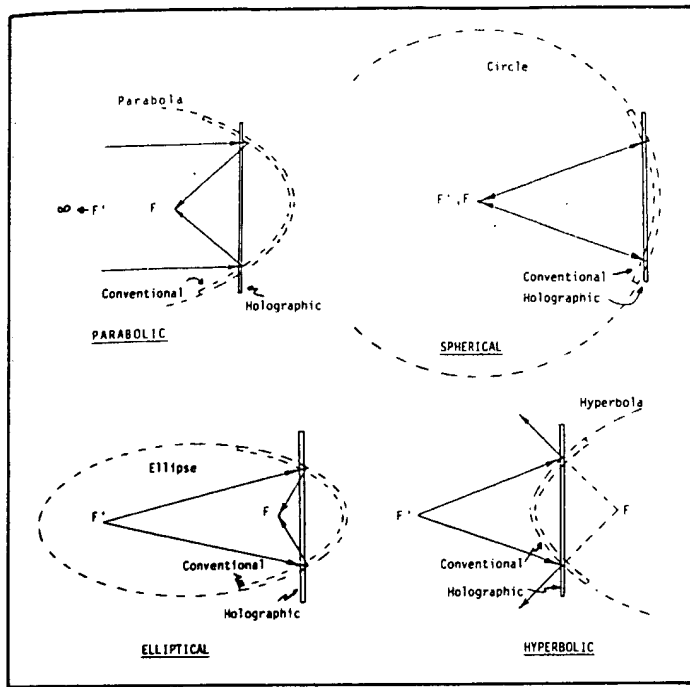


Fig. 1. Construction geometries. F and F' are (I) the foci of the conventional mirror, (II) the foci of the holographic mirror, (III) the foci of the geometric optic, and (IV) the spatial points at which the laser light converges or from which it diverges in the construction of the hologram.

2.4. Properties

Holographic mirrors are theoretically capable of producing perfect imagery. The simplest theoretical case for achieving this is when the reconstruction geometry is identical to the construction geometry: the point object is at the original point source location with identical wavelength and with no distortion of the recording medium.

A holographic mirror can image extended objects and diffract light at angles different from that of the original construction geometry or Bragg condition. The wavelength of illumination may be different, or not monochromatic, violating the Bragg condition. During processing, the film can be distorted by swelling, affecting the information registered. All of these variations will cause aberrations that must be corrected or compensated.

The properties of holographic mirrors include the following: (a) they can be produced by a photographic process; (b) their optical configuration is independent of the substrate configuration; (c) they can be spectrally selective, performing as narrowband rejection filters; (d) their efficiency is relatively insensitive to angles of incidence; (e) there can be more than one hologram on the same substrate, each performing with different characteristics; (f) they can perform multiple functions as optical windows, mirrors, and beam splitters; (g) their physical weight can be insignificant when compared to conventional optics; and (h) potentially, they are low cost in mass production, etc.

Properties that limit the usefulness of holographic mirrors in some systems are their high dispersion associated with the diffractive process and, for gelatin film holograms, their high hygroscopicity, which can cause alteration, or even destruction, of the performance of the hologram.

3. TECHNOLOGY

3.1. Materials

Gelatin film photosensitized with ammonium dichromate has been chosen as the best material, so far, for the production of holographic mirrors. It is the only material that can produce holographic mirrors with an efficiency very close to 100%, scattering of less than 1%, high spatial resolution, and durability in the

recording. The principal disadvantages are their relatively low sensitivity, which also is limited to the blue-green spectral region, and their hygroscopic nature.

The dichromated gelatin process has been extensively studied by the authors. Over 10,000 experimental holographic mirrors (in sizes from 10 cm \times 12.5 cm to 82 cm in diameter) were produced and evaluated with regard to different parameters in the formation of the gelatin film and the entire holographic process. The resulting technology offers a holographic mirror of repeatable quality with the high production yields needed for industrial applications.

3.1.1. Gelatin film

Commercially available gelatin film from photographic emulsions has been studied by others, such as Chang,⁶ in recording volume-phase transmission holograms. The limitations of these commercial films are their fixed parameters of particular thickness, initial hardness, and flat substrates of relatively small dimensions. As a consequence, the potential of the dichromated gelatin holographic process using these commercial films is restricted, and so the conclusions of the mentioned studies refer only to these films and cannot be generalized. Gelatin films produced in holographic laboratories can have different characteristics and thus produce results that are difficult to compare, replicate, and evaluate with regard to defining a best standard process. Processes that work very well with a particular gelatin may not be best suited for another.

The most significant parameter of a holographic gelatin film, in accordance with the process that is proposed below, is its initial hardness. The hardness of a gelatin film has been evaluated with respect to (a) the type of gelatin (acid or alkaline and its bloom), (b) the pH of the gel solution, (c) the gelation time, (d) the drying time, and (e) the chemical and thermal hardening (including in the other extreme the use of plasticizers). All of these parameters are interdependent and will define the gelatin hardness.

The rupture load and the water absorption of the film for a particular pH vary with type of gelatin. It has been found that an appropriate mixture of gelatin offers more versatility and produces results that are not achievable using any individual gelatin type. The pH of the gelatin solution has a strong influence on the gelation time and on the absorption of water, the resistance to rupture (reticulation), and its precipitation in isopropanol.

The gelation time is the most important parameter in determining the hardness of the gelatin film and the diffraction efficiency of the hologram. The drying time has a similar relationship and is used to obtain a more critical tuning of the hardness. The drying time also controls the flatness and uniformity of the film.

Hardening of the gelatin film using chemical hardeners, heat, or actinic radiation has generally been found undesirable since these are not as controllable as the previously mentioned parameters. They can contaminate the film causing nonuniformities and other side effects. The use of plasticizers to increase water absorption can also produce poor results, although they can be used to obtain a permanent swelling of the film (36% maximum swelling has been obtained).

The photochemical spectral sensitivity and the spectral response have also been investigated and developed. The original blue-green sensitivity has been extended to the red. Mirrors with a spectral response from the low ultraviolet to the infrared have been produced. This is achieved either by controlled permanent swelling of the film (physically changing the spacing between planes of diffraction) or by changing the angles between construction and reconstruction, or both. Another method is the use of the second or higher harmonics.

3.2. New dichromated gelatin process theory

The photochemical process is illustrated in Fig. 2. The molecular chains in the material are more cross-linked in the parts that have been exposed to light and become harder. The differential hardness between exposed and nonexposed parts causes a modulation of the index of refraction in the volume of the gelatin producing a three-

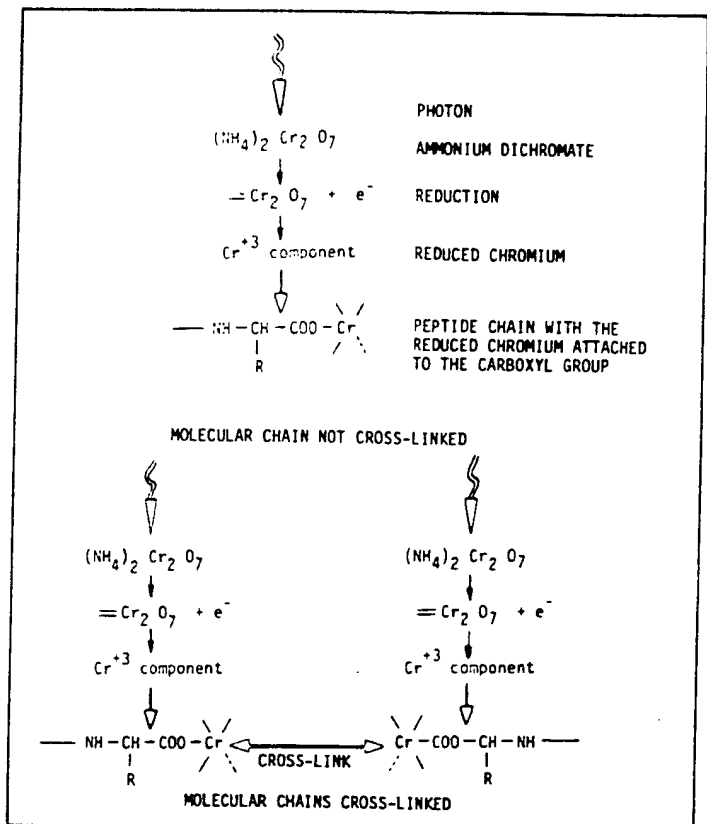


Fig. 2. Cross-link mechanism. Gelatin peptide chains with the carboxyl group attached to the photoreduced chromium.

dimensional grating or hologram. The original dichromated gelatin process for holographic application was proposed by Shankoff.⁷ He explained that high values of index modulation were obtainable by a fast dehydration of the film after it had been exposed to light and swelled with water. This theory cannot explain the very high values of diffraction efficiency (close to 100%) that require very large refractive index changes. Several additional theories have been proposed: (a) the voids and cracks by Curran and Shankoff,⁸ (b) chemical bonding of isopropanol by Meyerhofer,⁹ (c) the small air vacuoles by Case and Alferness,¹⁰ and (d) the molecular chain spring by Chang.¹¹ Each of these theories explains the behavior of particular holograms but is not adequate to form a general model. Graube¹² pointed out the possibility that gelatin can react differently to processing, depending on its hardness and other parameters.

The new theory¹³ proposed here is more general in explaining the different efficiencies and noise in the holograms. It is based on the experimental observations of the reaction between isopropanol and different concentrations of gelatin. Graube reported that gelatin can be precipitated by the alcohol, forming amorphous aggregates. Not only does this occur but, depending on the state of the gelatin, the alcohol will produce no precipitates or precipitates of different transparency. Most importantly, it can produce an isopropanol-gelatin gel that remains after the film is processed and dried.

The new theory is illustrated in Fig. 3. The gelatin, after it has been exposed and washed, is in a swollen state, the swelling being proportional to the initial hardening of the gelatin and the energy in the exposure. When the gelatin is introduced in the isopropanol bath, different reactions can occur. A gelatin is classified as very soft when the parts that have been exposed to less light become very dilute during the wash and develop into a highly expanded volume (contained by the harder nondiluted gel, which has received more light). In the alcohol bath, the gelatin in this very dilute solution is precipitated as opaque amorphous grains. When the film is dried and the alcohol evaporates, the gelatin grains form internal cracks,

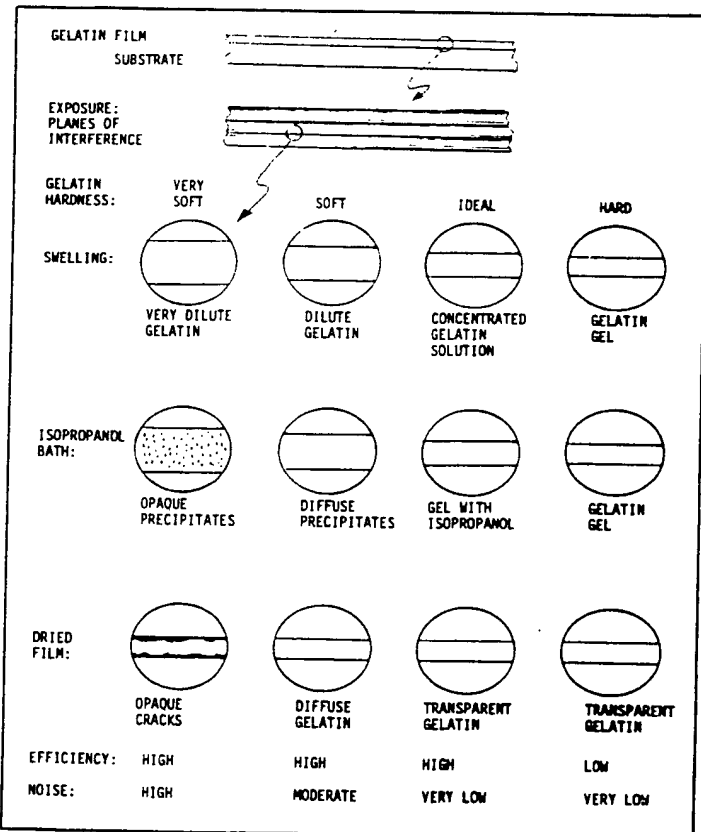


Fig. 3. New model for the dichromated gelatin process. Isopropanol interaction with gelatins of different hardness.

causing large noise (scattering) and producing high efficiencies due to the large index modulation between the solid gelatin and the air in the cracks.

A gelatin is classified as very hard when it swells during the washing but remains in a gel state without forming a solution. In this case the isopropanol will not precipitate or modify the gelatin, but produces a fast dehydration that, depending on the variation in swelling, will cause local strains. When the film dries, these strains will alter the index of refraction, but the value of this index modulation can only produce low diffraction efficiencies. Without gelatin precipitates or reticulation, these holograms are free of scattering. Hard gelatins are consistent with the first model proposed by Shankoff.

A gelatin has an ideal hardness when the parts exposed to less light are dissolved, but the solution is highly concentrated. In this high concentration the gelatin is not precipitated by the isopropanol but forms a gelatin-isopropanol gel that is completely transparent and remains in this state after the film is dried, even to temperatures as high as 100 °C. The index of refraction of the (low density) gelatin-isopropanol gel is very different from the index of the (high density) solid gelatin in the parts that have received more light. This large refractive index variation will produce an index modulation to account for the highest diffraction efficiencies in low noise holograms.

Experiments of the reaction of isopropanol and different concentrations of gelatin solution, gel, and solid gelatin, Fig. 4, have proven the formation of opaque grain precipitates, of more or less diffuse amorphous precipitates, and of the transparent gel containing isopropanol, and they have proven the absence of alcohol-gelatin interaction when the gelatin is in solid or gel state.

4. HOLOGRAPHIC MIRROR CHARACTERISTICS

The characteristics of holographic mirrors are related to the par-

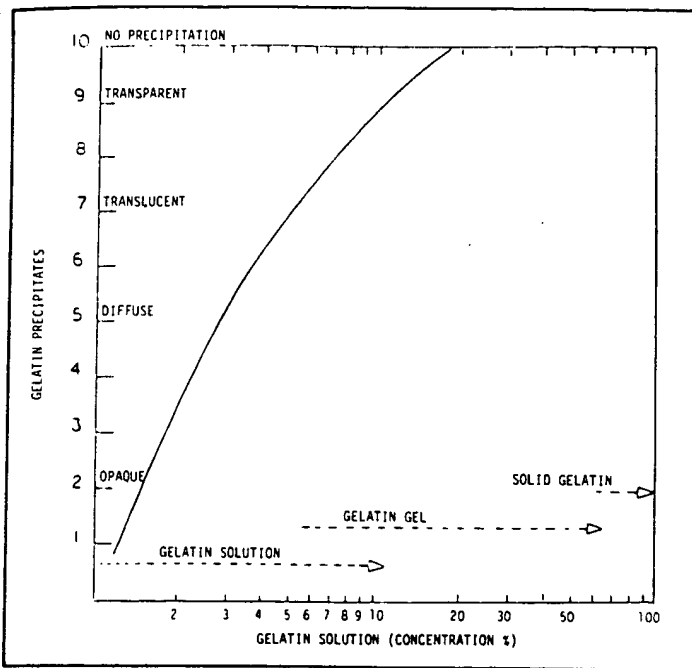


Fig. 4. Gelatin precipitates from gelatin solutions with isopropanol.

ticular application or optical system in which they are used. The relative importance of each can vary, but usually the following characteristics are considered.

4.1. Diffraction efficiency

The diffraction efficiency (DE), i.e., "reflectivity," of a holographic mirror is the end product of most of the investigation in the holographic mirror technology. The characteristics of the gelatin film, thickness, origin, and initial hardening, and every step in the process including the deposition of the film, the aging, the photosensitization, exposure, developing, drying stabilization, and sealing will have an important influence on obtaining holograms with good repeatability and a desired diffraction efficiency. The desired diffraction efficiency is difficult to achieve in particular applications where it must be controlled to precise values (as in beam-splitter mirrors where $DE = 50\%$, $T = 20 \mu\text{m}$, and $n_1 = 0.008$) or where it must be extremely high (as in the production of holographic notch filters with high optical densities or high power laser mirrors where $DE = 99.999\%$, $T = 20 \mu\text{m}$ and $n_1 = 0.056$).

The gelatin used was chosen by knowing (a) its resistance to rupture when it is in the gel state, (b) the time of gelation and film deposition drying, and (c) the capacity of water absorption and swelling. Although these characteristics were originally studied independently, they are interrelated and are of great importance in obtaining holograms with high diffraction efficiency and low noise. The maximization of these gelatin properties was achieved by using a mixture of gelatins.

The concentration of ammonium dichromate is critical in holographic mirror production due to the incidence of interfering waves from opposite sides of the film. Large concentrations will produce crystallization over the surface of the film or high levels of absorption, changing considerably the interfering beam ratios. Very small concentrations will cause low absorption and inefficient photochemical effects. Large concentrations of dye in thick films are also difficult to wash out. Construction geometries using two independent beams will require different concentrations than other geometries, such as the back mirror geometry, in which one interfering beam crosses the film twice.

Long storage of the film after being photosensitized is detrimental because of a dark reaction. Storage of many months at room temperature will lower the diffraction efficiency, but it will still be

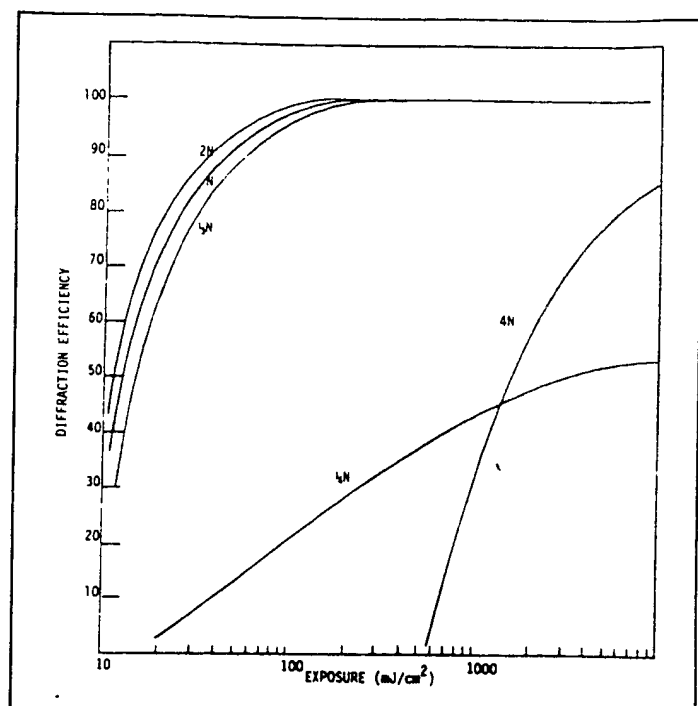


Fig. 5. Variation of the diffraction efficiency with relation to the exposure for films of various thickness ($N = 20 \mu\text{m}$) with varying absorption due to constant dye concentration.

over 90% for well-prepared films.

The low sensitivity of the dichromated gelatin requires relatively long exposure times, particularly for large size holographic mirrors. Instability problems, if not quite noticeable for their severity, can lower the contrast between maxima and minima of interference and reduce the diffraction efficiency. Contrast reduction will also occur with very different intensity beam ratios. Curves in Fig. 5 show diffraction efficiency versus exposure energy for films of different thickness and the same concentration of dichromate and, in Fig. 6, for different thicknesses but having the same absorption values.

The development of the film is basically that proposed by Shankoff.⁷ Avoidance of film contamination and control of the pH are essential. Dehydration by isopropanol must be complete, and the development temperatures must be in accordance with the hardness of the gelatin.

4.2. Spectral response

The spectral response of holographic mirrors is relatively monochromatic. Its location in the spectrum is dependent on the construction wavelength, the construction-reconstruction angles, the characteristics of the gelatin, and the effects of environmental parameters throughout processing and in the final sealing. The Bragg law establishes the dependence of wavelength on the construction and reconstruction angles and on the spacing of the planes of diffraction. In the dichromated gelatin wet process, swelling of the gelatin can produce an undesirable spectral shift or can be controlled to obtain a desired one. The ratio between the volume of the gelatin during the exposure and the final hologram volume is not only affected by the immersion of the gelatin in water and dehydration but also by the environmental humidity conditions until the hologram is properly sealed. Holographic mirrors from 340 nm (limited by the gelatin absorption) to 3.1 μm (limited by the 20 μm film thickness that we have used) have been produced with high diffraction efficiencies.

4.3. Spectral bandwidth

The spectral bandwidth $\Delta\lambda$ of holographic mirrors is related to the diffraction efficiency and other gelatin parameters by the equations

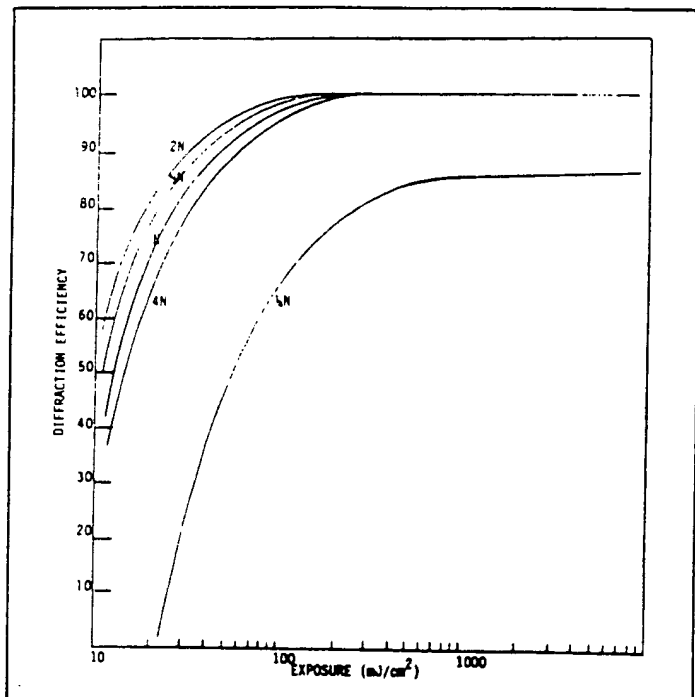


Fig. 6. Variation of the diffraction efficiency with relation to the exposure for films of various thicknesses ($N = 20 \mu\text{m}$) with constant absorption due to varying dye concentration.

mentioned before. Experimental spectral bandwidths do not always agree with the theoretical values. The discrepancy is attributed to what is called the "envelope" bandwidth, in which secondary maxima are considered, and to a deformation of the grating, similar to a chirped grating in which the period of the grating is not constant. We have recently reported experimental evidence of these effects.¹⁴ The experimental bandwidth obtained in our holographic mirrors is controllable from about 10 nm to over 200 nm. Bandwidths larger than 200 nm are produced with relatively soft gelatins, and they have some scattering.

4.4. Optical properties

Holographic mirrors, as compared with conventional mirrors, have the same type of aberration, which in some cases can be more severe. Figures 7 and 8 illustrate this in a spherical mirror. The imagery can be perfect when the holographic mirror is used in the same geometry in which it was constructed and with the same monochromatic illumination.

Besides the general optical properties mentioned in the introduction, holographic optical mirrors (volume-phase reflection holograms) also have the following properties: (a) there is only one image, real or virtual, for each orientation of the hologram; (b) higher order images are nonexistent or are of very low intensity; and (c) the angular selectivity is very low (thereby not restricting the field of view of the holographic mirrors).

The general theory of image formation is developed in accordance with the holographic process, considering the construction and reconstruction parameters and the laws of diffraction. For a conventional mirror, the paraxial approximation considers the rays near the optical axis. For a holographic mirror, this approximation will consider the rays near the axis coincident with the directions of incidence of the object and reference beams (Bragg condition), which define a biaxial system. An analytical formulation considering paraxial rays in systems without symmetry has been given by Rose.¹⁵ Champagne¹⁶ also considers the nonparaxial case. Analytical approximations have been proposed by Close,¹⁷ Arsenault,¹⁸ Sweat,¹⁹ and others. The final design of our holographic mirrors has been made using a ray-tracing program,

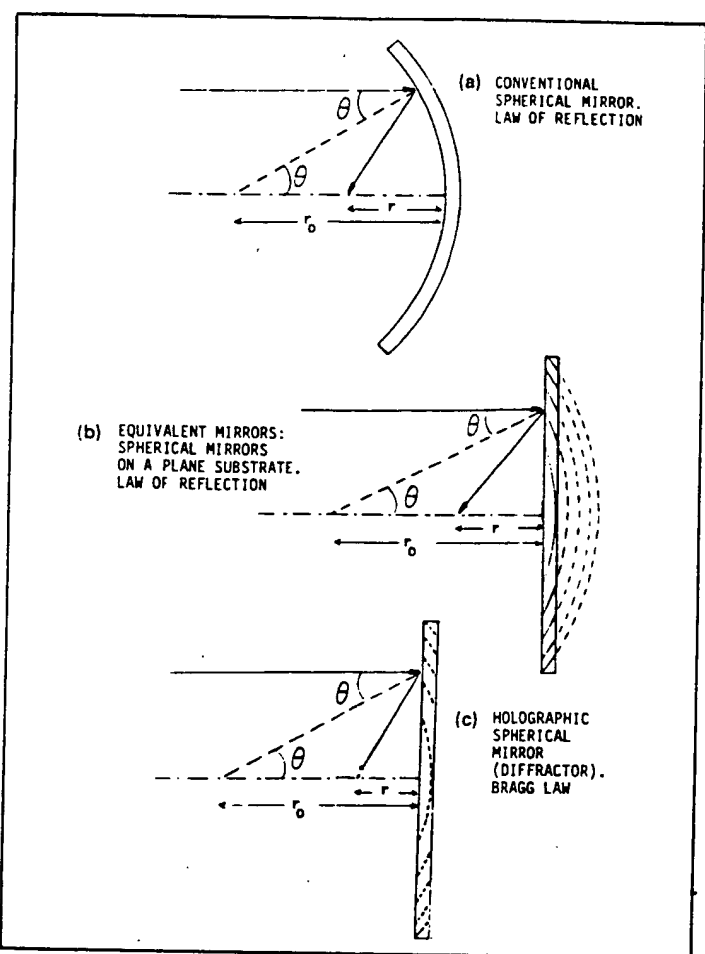


Fig. 7. Geometries to compare spherical aberration.

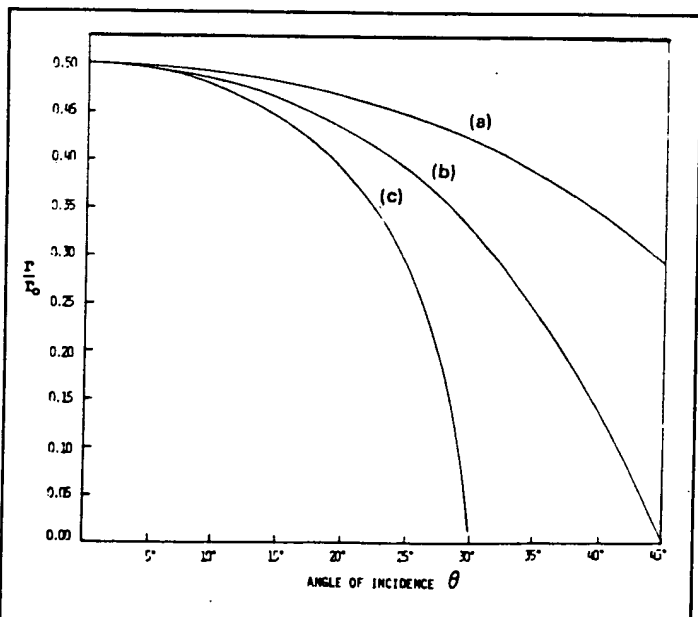


Fig. 8. Spherical aberration for the mirrors of Fig. 7.

specifically the HOAD (holographic optics analysis and design) initiated by Latta²⁰ and developed by the Environmental Research Institute of Michigan. Examples of experimental and computed results are given in Fig. 9 for a spherical holographic mirror with a focal length of 50 cm and a maximum aperture of 82 cm. Figure 10

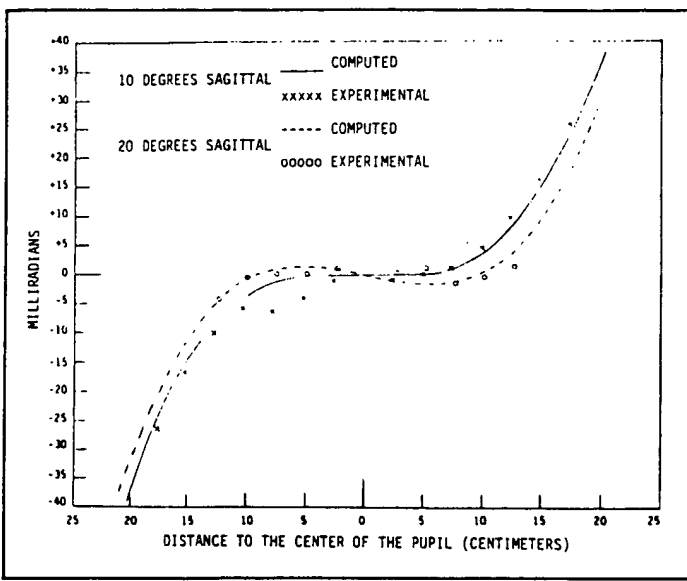


Fig. 9. Computed and experimental values of decollimation for a holographic spherical beam-splitter mirror.

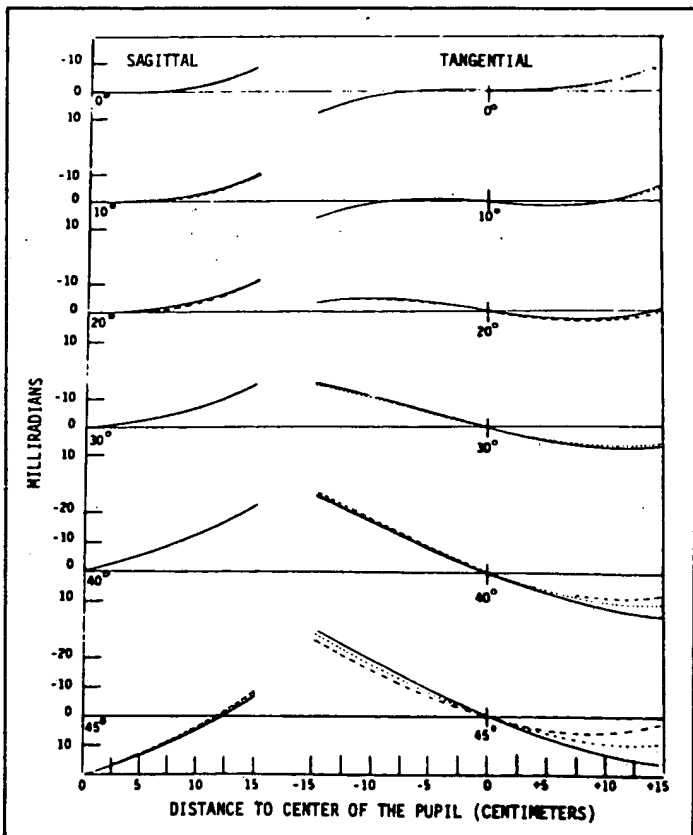


Fig. 10. Decollimation values for a compound (blue, green, red) holographic aspherical beam-splitter mirror.

gives the design values (by Farrand Optical Design group) of a tricolor holographic aspherical mirror ("white" response hologram) with a focal length of 53 cm and a maximum aperture of 106 cm. An earlier experimental model of this mirror and its color rendition are shown in Fig. 16.

Peculiar to the optical quality of holographic mirrors are cosmetic defects and ghost images. Clean room facilities and extreme care are needed to avoid these defects, and special tooling is required in the construction geometry to avoid multiple internal

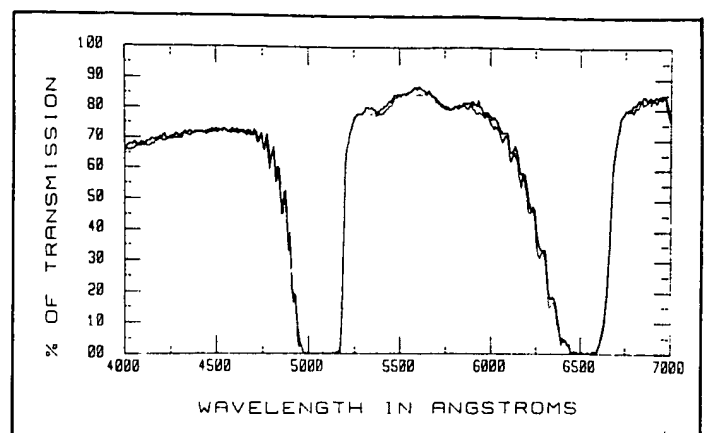


Fig. 11. Holographic dual-notch filter: Spectral response before and after environmental test. (Curves are practically superimposed on each other.)

reflections or stray light that can produce secondary holographic recordings and ghost images.

4.5. Endurance of the holographic mirrors

Holographic mirrors must be stabilized with regard to changes in temperature, which can produce a spectral response shift. They also need to be sealed from moisture, which not only can produce a spectral shift but can also reduce or annul the diffraction efficiency. Holographic mirrors produced by the authors have been stabilized to temperatures close to 100 °C and have been successfully sealed to pass immersion in water and temperature and humidity tests (Fig. 11).

Another aspect of the endurance of holographic mirrors is their resistance to radiation. The low absorption of the gelatin film and their high "reflectivity" make them potentially more resistant than conventional mirrors. Initial experiments have demonstrated a survivability on the order of MW/cm^2 for our holographic mirrors with focused cw argon lasers and similar energies with short-pulsed infrared lasers.

5. FACILITIES

The development of gelatin films for producing very large size (to 1.5 m) holographic spherical beam splitters and the control and repeatability of the dichromated gelatin process required special holographic facilities, which were built in 1976 based on the knowledge from several years of previous research.²¹

The self-enclosed six rooms of the Research and Development Holographic Laboratory are of 10,000 class clean room quality (less than 10,000 particles larger than $0.5 \mu m/ft^3$), and the gelatin film coating booth is of 100 class quality.

The entire laboratory has temperature controls with tolerances of $\pm 1^\circ C$ and humidity controls with $\pm 5\%$ relative humidity. Water is distilled and demineralized. Purity of the chemicals is controlled. The temperatures of water and solutions have tolerances of $\pm 0.25^\circ C$.

The laboratory has a cw argon laser, Spectra Physics model 171, and a krypton laser, Spectra Physics model 171. For measurements and monitoring there are also He-Ne lasers and a YAG laser, which can be frequency doubled. Spectral measurement and analysis are made with a Perkin-Elmer spectrophotometer model 330 and an adapted Farrand Mark III spectrofluorometer with a double monochromator. A spot Pritchard photometer and Farrand photometers are also used.

The laser and exposure rooms are separated and vibrationally and acoustically insulated. The master conventional spherical mirror used for construction of large holograms has a maximum dimension of 144 cm. An immersion cell of similar dimensions is used to avoid internal reflections in the construction geometry.

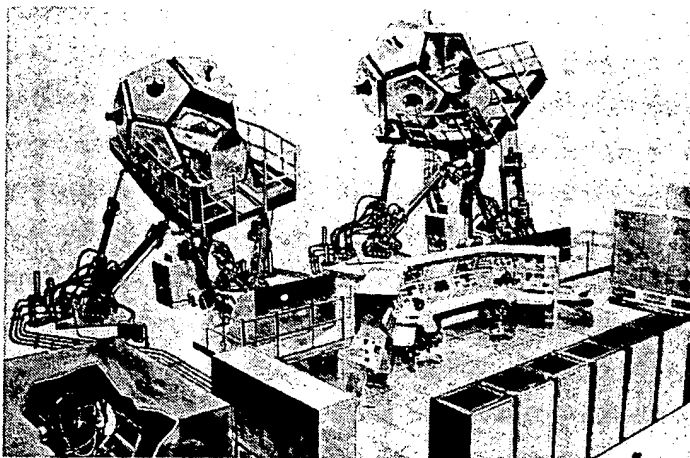


Fig. 12. Pilot training-simulator with dodecahedron Pancake Window configuration.

Several plane, prismatic, and other configuration cells are used for smaller holograms.

6. APPLICATIONS

Holographic mirrors are not making conventional mirrors obsolete, nor will they replace them in most optical systems. But, in some systems or applications they can have particular advantages. For example, the advantages of low weight and low production cost can be a trade-off for some optical quality. For monochromatic illumination, holographic mirrors can achieve equal or better optical quality than conventional mirrors. The same applies for optical configurations in which the holographic construction-reconstruction parameters are not changed (Bragg's law condition). Holographic mirrors can "reflect" light by diffraction in directions and in configurations that would be impossible for a conventional mirror. The performance of multiple functions provides specific advantages such as would be the case for multiple holographic mirrors stacked in the same substrate or for a holographic mirror and its substrate acting as a transparent window and a spherical mirror. Proposed and actual applications of holographic mirrors have been numerous, and those which Farrand Optical Company has developed and used will be described: holographic spherical and aspherical beam-splitter mirrors of large dimensions for optical simulators, holographic notch filters for eye and instrumentation protection against laser radiation, and holographic combiners for head-up systems.

6.1. Holographic Pancake Window

This system has already been described²² with particular emphasis on its simulation and optical engineering aspects but not on its holographic characteristics and performance. The Pancake Window is an optical magnifier that displays, to an observer, images at optical infinity. With regard to an optical simulator for aircraft pilot training, etc., it has the advantage that images at the optical infinite correspond better to images that we observe in the outside world. Since it is a magnifier with only on-axis reflective optics, it provides a very large field of view with good optical quality and without (in the conventional mirror version) chromatic aberration. In the holographic version, a spherical beam-splitter mirror is replaced by a holographic mirror with the goal of reducing the weight of this system by 75% and the cost by approximately the same percentage. Due to the very large size and cost of these systems, Fig. 12, the potential for savings is considerable.

The Pancake Window configuration and components are represented in an exploded view in Fig. 13. The polarizers and quarter-wave plates have the function of blocking the direct vision of the object (screen), which, without them, would be transmitted through the two beam-splitter mirrors. In the holographic

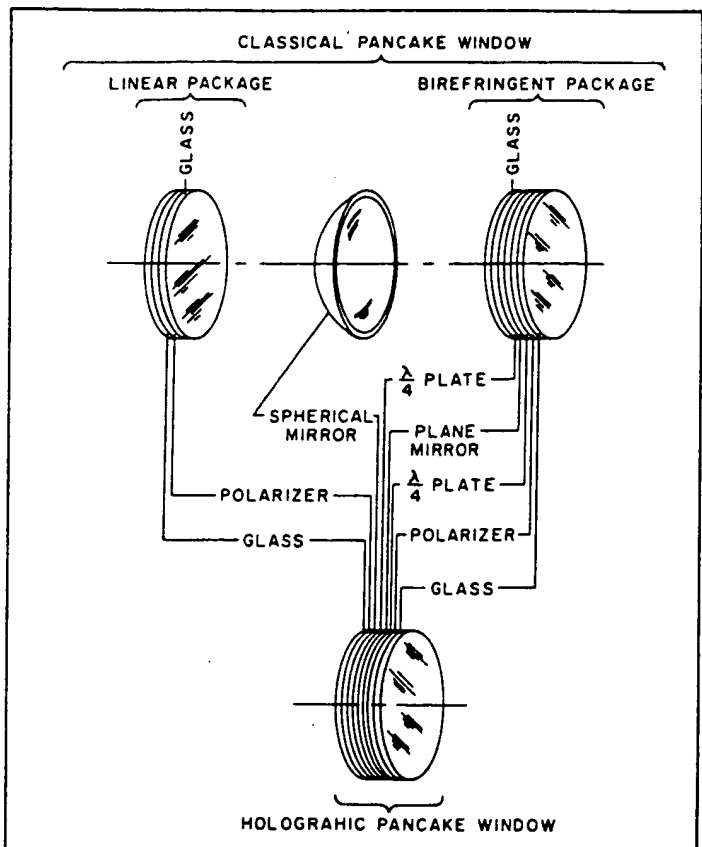


Fig. 13. Compactness of the holographic Pancake Window.

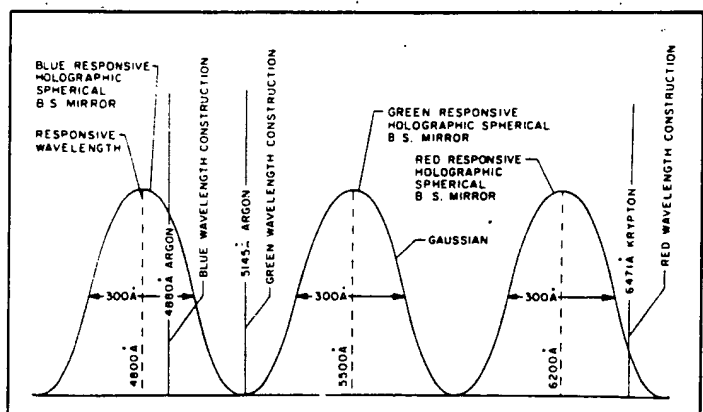


Fig. 14. Laser lines for hologram construction and hologram wavelength response.

"monochromatic" version the holographic beam-splitter spherical mirror is designed to operate with a wide bandwidth illumination CRT phosphor and a narrow response holographic mirror. This will control the dispersion and allow reasonable optical resolution in very large field-of-view systems (over 90°). For systems with smaller field-of-view requirements, a narrow spectral phosphor input, such as the P-44 phosphor, can be combined with a wide spectral response holographic mirror, in which case the phosphor controls the dispersion. The optical performance (collimation) of one of these mirrors is represented in Fig. 10.

For color display, a compound holographic spherical mirror²³ was originally designed, consisting of three mirrors having narrow spectral responses in the blue, green, and red, respectively (Fig. 14). This combination produced a wide spectral response performance and simultaneously controlled the dispersion, which in a

single wide-response hologram would be intolerable. The focal length, and consequently the magnification of the holographic Pancake Window diffractive mirrors, is a direct function of the wavelength used in the illumination. To compensate for this effect, the mirrors were constructed with different centers of curvature considering the construction-reconstruction wavelengths and the desired common focal length of the holographic compound mirror (Fig. 15). The color rendition of one of the earliest experimental windows is represented in Fig. 16. The performance of a better aspheric design was mentioned earlier (Fig. 10).

6.2. Holographic notch filters

An optical notch filter rejects light over a narrow selected band of frequencies and allows a maximum overall transmission outside the rejected band. The most developed (nonabsorption) types have a basic multiplane or multilayer configuration, and they have the common characteristics that (a) the narrower the rejected band of frequencies, the larger the number of planes required; (b) maximum transmission outside the rejected frequency requires the elimination of side lobes by small index modulation between planes; and (c) the rejected frequency shifts with the angle of incidence.

The holographic notch filter can be considered the closest to the ideal since it has a large number of diffraction planes (about 160 in 0.03 mm thick film for 550 nm wavelength) and has a relatively small modulation index (about 0.05). Most importantly, it is the only filter that, for particular geometries, can be almost independent of the angles of incidence.

The principal parameters that specify a notch filter are (a) the spectral location of the rejection band for a particular angle of incidence; (b) the optical density, the amount of light that will be rejected, or the protection obtainable with the filter; (c) the protection not only for a particular angle of incidence but for a field of view or angular coverage; and (d) the transmission outside the rejection band that must be maximized if observation through the filter is to be spectrally undistorted and without significant attenuation.

The most common material for producing these filters is dichromated gelatin with efficiencies of rejection larger than five in optical density units (10^{-5} of the rejected light is transmitted). The rejected band frequency shifts with the angle of incidence. The shift is not linear but increases slowly for small angles of incidence, becoming faster for large angles. The theoretical shift calculated with the Bragg law is in accordance with the measured experimental shift. The bandwidth of the notch (the rejected band) for the holographic filter has an apparent discrepancy between theoretical and experimental values, the latter being larger due to effects in processing the film and in photometrically reading not the first maximum at the half intensity points but the envelope of the curve containing secondary maxima. The ideal square wave notch, while theoretically achievable with a proper index modulation and thickness, is not experimentally feasible. As a consequence, to compensate for a shift of the notch, the bandwidth required becomes wider as the optical density rises. Experimental data indicate that, for example, to maintain an optical density of 4 throughout a shift of 15 nm, the bandwidth of the notch needs to be 28 nm instead of around 18 nm for a close to square wave notch.

For eye protection, the scotopic or photopic transmission will be affected by the spectral position and bandwidth of the notch. Large angles of incidence produce large shifts of the notch, and to compensate for it, wide bandwidth notches are required, resulting in low transmission. The incompatibility of large field coverage and high photopic or scotopic transmission can be avoided using some unique holographic properties.²⁴

The optical figure of a holographic mirror does not need to be the same as the geometrical figure of the substrate. Plane, spherical, or aspheric holographic mirrors can be produced on a plane or any other substrate. All that is required is that in producing the hologram the wavefronts reaching the substrate (on which the film is deposited) converge or diverge from spatial points coincident

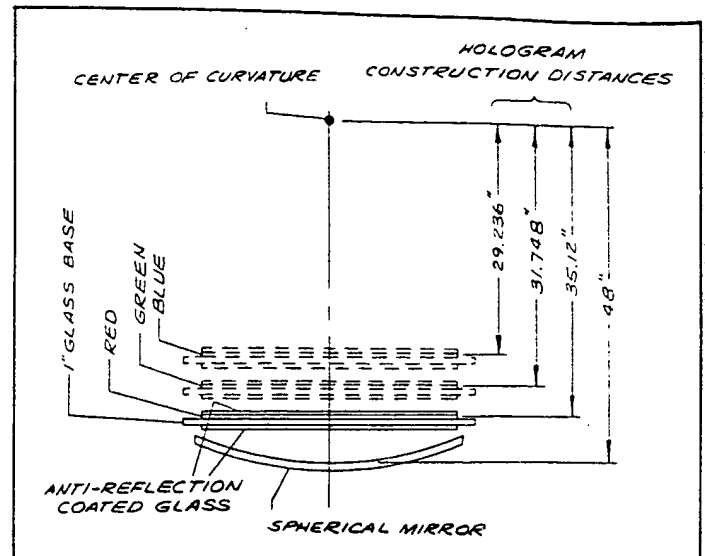


Fig. 15. Construction geometry for the compound (blue, green, red) holographic spherical beam-splitter mirror.

with the foci of the correspondent conic. These geometrical foci will become the foci of the optical holographic mirror (Fig. 1).

Therefore, in a holographic notch filter used on a spectacle lens, the optical configuration of the holographic mirror (filter) does not need to be coincident with the geometrical shape of the spectacle. If the holographic notch filter has the optical configuration of a spherical mirror with its center of curvature coincident with the center of rotation of the eye, then all the rays incident toward the center of the eye will be normal to the holographic mirror and will have a constant 0° angle of incidence. The size of the pupil of the eye and the rotation of the eye force allowances to be made for the small angles of incidence incurred, and the ideal case of constant 0° incidence is not practically possible. Still, these small angles, $\pm 9^\circ$ at the center and about $\pm 16^\circ$ at the edges, will not reduce significantly the photopic or scotopic transmission (Fig. 17). (There is a U.S. patent application on file for the above.)

The difference between an optically plane holographic mirror and a holographic spherical mirror notch is that there is no shift in the spherical case. This allows the notch to be constructed with a bandwidth that maximizes the scotopic or photopic transmission. The experimental curves of a plane holographic notch (equivalent to the dielectric multilayer filter) on a plane substrate show a shift of the notch of 70 nm for a 45° angle of incidence. For a protection of 4 optical density throughout these angles, the required notch bandwidth will be about 90 nm with a photopic transmission of about 40%. For the case of the spherical mirror holographic notch, on a plane lens substrate, the shift is less than 5 nm. A bandwidth of 15 nm will allow a photopic transmission of about 85% (Fig. 18).

Approaches similar to the spectacle-eye geometry can be applied in the case of goggles, etc. For the case of goggles, a holographic elliptical mirror with each of its foci at the center of an eye will achieve total field coverage. The size of the pupil will again require small angle of incidence tolerances, as those described in the spectacle-eye geometry (Fig. 19).

Multiple holographic notches can be superimposed on the same substrate and offer protection for more than one discrete frequency. Still the transmission between these rejected frequencies is very large due to the absence of side lobes and secondary maxima. Holographic notch filters anywhere from 340 nm to $3.1 \mu\text{m}$ have been produced on plane and curved substrates (glass or plastic) (Fig. 20).

6.3. Holographic combiners

A holographic combiner is defined as a dual-function optical ele-

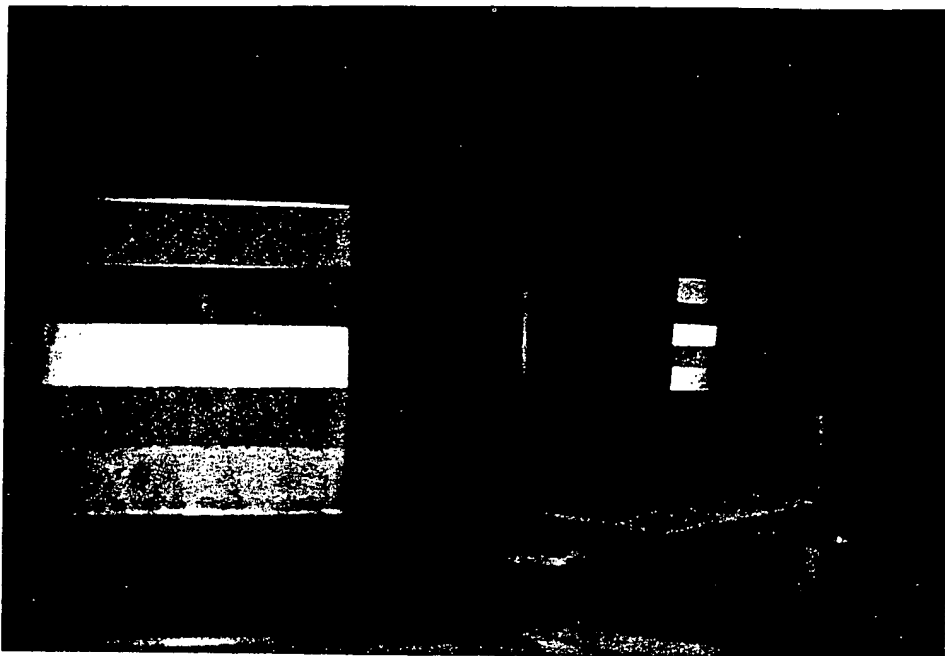


Fig. 16. (a) Color rendition of an experimental holographic tricolor Pancake Window.

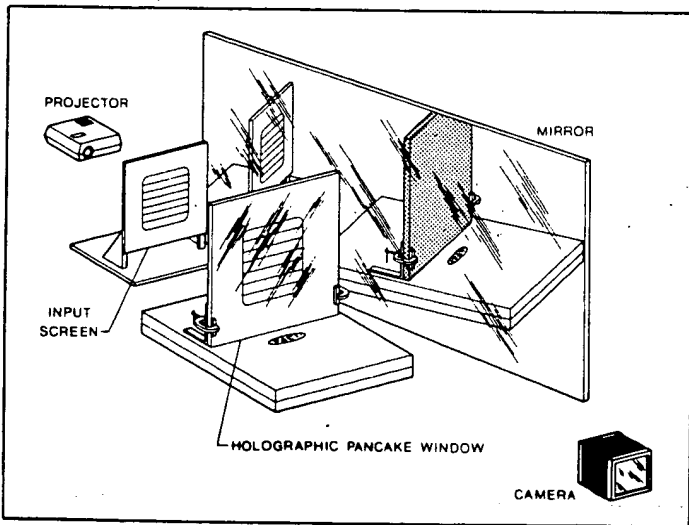


Fig. 16. (b) Schematic of photographic setup for (a).

ment that simultaneously performs as an optical window (nearly undistorted transmitted images) and as an analog of a conventional lens or mirror. They are used primarily in applications (as in head-up systems) in which analog or digital information is superimposed on images transmitted by the system (as the images of the real world). Most of the desired characteristics of a combiner can be improved holographically, and even new configurations become feasible. Conventional combiners are beam-splitter mirrors with or without curvature.

The spectral selectivity of the holographic combiner allows higher transmission values and less distortion of colors. A narrow bandwidth notch can reflect nearly 100% of the display information and also transmit most of the light of the outside world. A conventional beam splitter with a wide spectral response operates with higher transmission losses.

The independence of the optical figure of the holographic combiner from the substrate allows the use of spheric or aspheric holographic mirrors coated on plane or curved substrates, as, for example, the pilot visor. The independence from the law of reflection

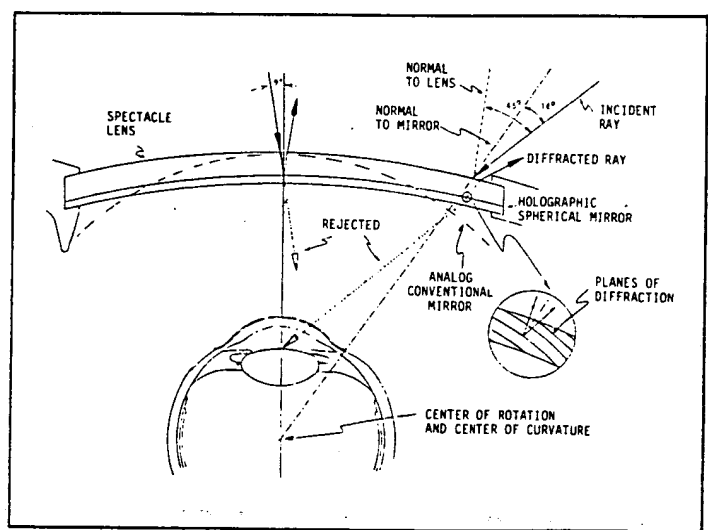


Fig. 17. Spectacle-eye geometry with a holographic spherical notch filter providing wide angular protection.

allows reflected images that would be impossible with conventional mirrors.

The field of view achievable with a holographic combiner may be limited because of the frequency shift associated with angles of incidence in the diffractive optics. Nevertheless, the possibility of better aberration correction with holographic aspherics or the use of multiple-element combiners, feasible only with holographic optics, allows designs that can provide larger fields of view than any conventional combiner system.

The configurations sketched in Figs. 21 and 22 are holographic combiners deposited on the actual pilot visor. These aspheric holographic mirrors will project at the optical infinite the images displayed on the overhead or side CRT projection system. A system that will superimpose the images obtained with an image intensifier or infrared system to the direct vision images is sketched in Fig. 23.

Farrand Optical applications of holographic combiners are in experimental prototypes for use in actual aircraft or in simulators.

Head-up system combiners have been produced and evaluated in

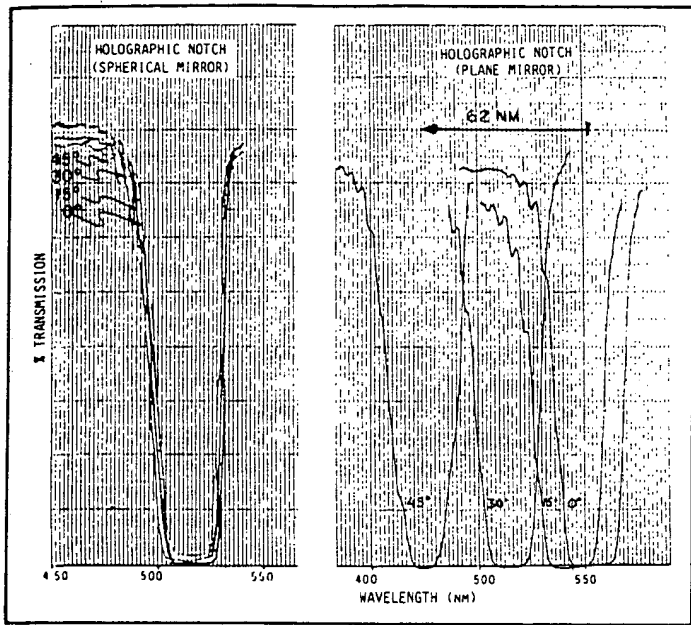


Fig. 18. Spectral shift with angle of incidence for a holographic spherical mirror (Fig. 17) and for a holographic plane mirror (multilayer analog) in the spectacle-eye geometry.

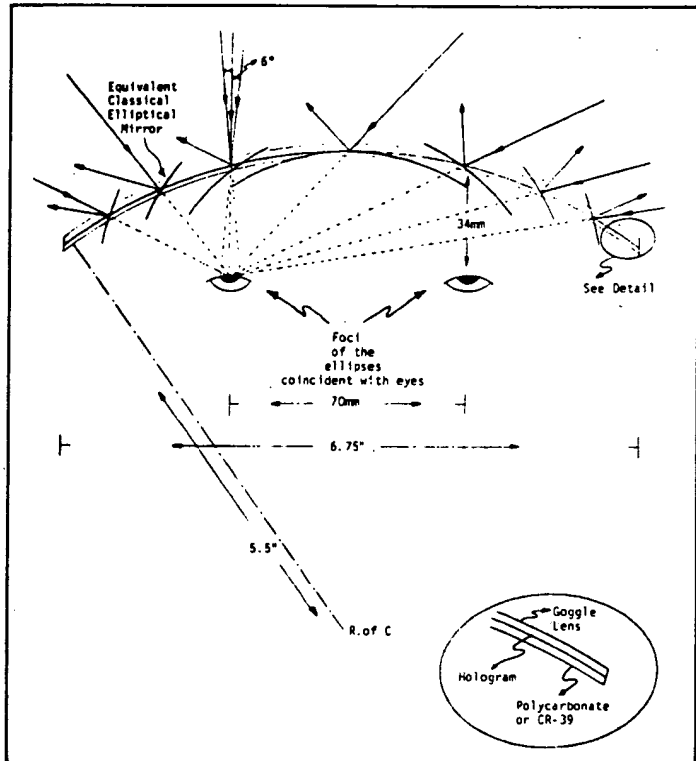


Fig. 19. Goggle-eye geometry with a holographic elliptical notch filter providing wide angular protection.

holographic analogs of conventional plane beam-splitter combiners and in analogs of aspheric systems, such as the one in Fig. 24.

7. CONCLUSIONS

Holographic mirrors in the applications mentioned in this paper are no longer laboratory curiosities but actual hardware used in industrially produced optical systems. This technology started with the low efficiency reflection zone plate and developed, particularly



Fig. 20. Triple-notch holographic filter on polycarbonate visor.

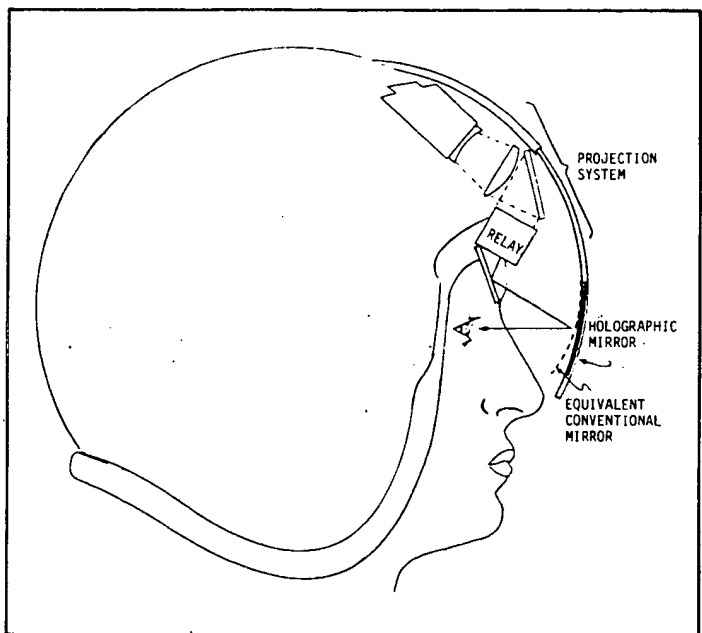


Fig. 21. Visor with a holographic elliptical mirror.

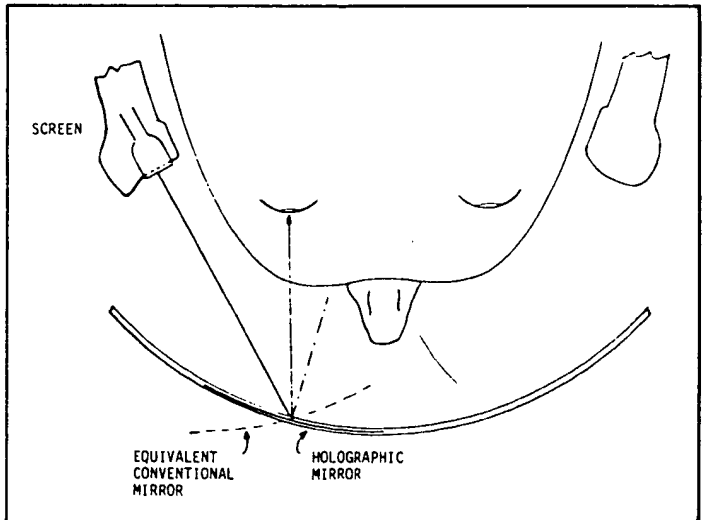


Fig. 22. Visor with an off-normal holographic spherical mirror. Side projection CRT.

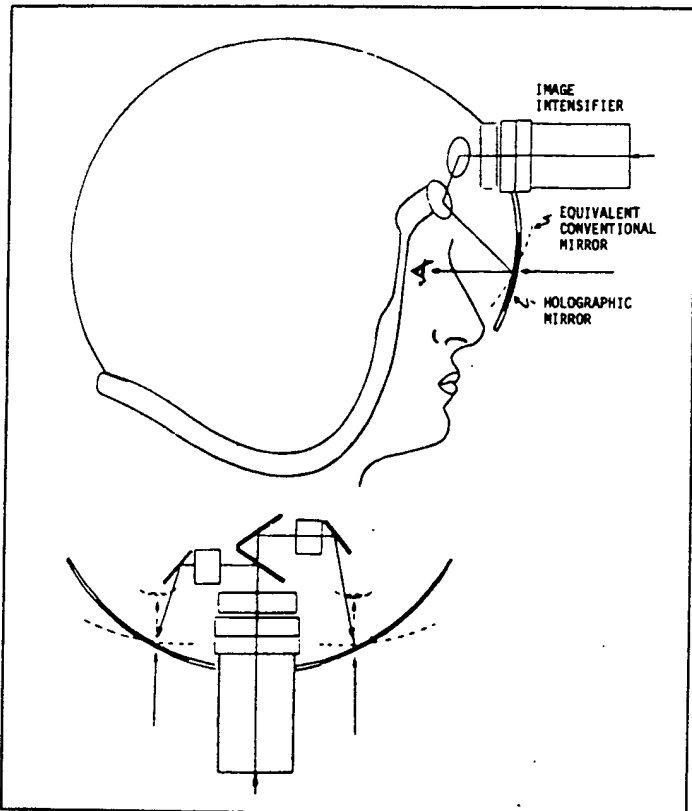


Fig. 23. Visor with holographic mirrors and Image Intensifier.

with the dichromated gelatin process, into very high efficiency mirrors worth being considered in optical designs and produced with a quality and repeatability to justify their implementation in actual optical systems. Development tasks will continue in the search for new and better materials, theoretical and optical designing knowledge, and other, yet to be discovered applications.

8. REFERENCES

1. R. J. Collier, C. B. Burckhardt, and L. H. Lin, *Optical Holography*, Academic Press, New York (1971).
2. L. Solymar and D. J. Cooke, *Volume Holography and Volume Gratings*, Academic Press, London (1981).
3. T. K. Gaylord and M. G. Moharan, *Appl. Phys. B* 28, 1 (1982).
4. H. Kogelnik, *Bell Syst. Tech. J.* 48, 2909 (1969).
5. H. M. Smith, *Holographic Recording Materials*, Springer-Verlag,

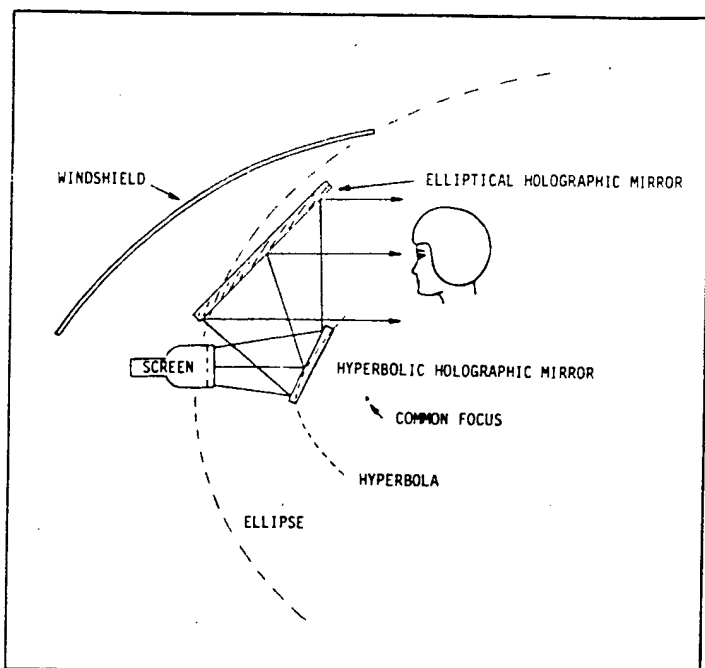


Fig. 24. Head-up system with aspheric holographic mirrors.

New York (1979).

6. B. J. Chang and C. D. Leonard, *Appl. Opt.* 18, 2407 (1979).
7. T. A. Shankoff, *Appl. Opt.* 13, 2942 (1974).
8. R. J. Curran and T. A. Shankoff, *Appl. Opt.* 9, 1651 (1970).
9. D. Meyerhofer, *RCA Rev.* 33, 110 (1972).
10. S. K. Case and R. Alferness, *J. Appl. Phys.* 41 (1976).
11. B. J. Chang, *Opt. Eng.* 19, 642 (1980).
12. A. Graube, *Proc. SPSE 32nd Conf. Boston* (1979).
13. J. R. Magariños, "Holographic Mirrors," Ph.D. Dissertation, Univ. of Santiago, Spain (1984).
14. D. J. Coleman and J. R. Magariños, *J. Opt. Soc. Am. A1*, 1221 (1984).
15. M. W. Rose, "Holographic Lens Systems," Ph.D. Dissertation, Ohio State Univ. (1972).
16. E. B. Champagne, *J. Opt. Soc. Am.* 57, 51 (1967).
17. D. H. Close, *Opt. Eng.* 14, 408 (1975).
18. H. H. Arsenault, *J. Opt. Soc. Am.* 65, 903 (1975).
19. W. C. Sweat, *Appl. Opt.* 17, 220 (1978).
20. J. N. Latta, *Appl. Opt.* 10, 599 and 609 (1971).
21. J. R. Magariños, *J. Opt. Soc. Am.* 67, 1374 (1977).
22. J. A. LaRussa and A. T. Gill, in *Visual Simulation & Image Realism*, Leo Beiser, ed., *Proc. SPIE* 162, 120 (1978).
23. J. R. Magariños, *Proc. ICO-11*, 415, Madrid, Spain (1978).
24. J. R. Magariños and D. J. Coleman, *J. Opt. Soc. Am. A1*, 1221 (1984).

**This Page is Inserted by IFW Indexing and Scanning
Operations and is not part of the Official Record**

BEST AVAILABLE IMAGES

Defective images within this document are accurate representations of the original documents submitted by the applicant.

Defects in the images include but are not limited to the items checked:

BLACK BORDERS

IMAGE CUT OFF AT TOP, BOTTOM OR SIDES

FADED TEXT OR DRAWING

BLURRED OR ILLEGIBLE TEXT OR DRAWING

SKEWED/SLANTED IMAGES

COLOR OR BLACK AND WHITE PHOTOGRAPHS

GRAY SCALE DOCUMENTS

LINES OR MARKS ON ORIGINAL DOCUMENT

REFERENCE(S) OR EXHIBIT(S) SUBMITTED ARE POOR QUALITY

OTHER: _____

IMAGES ARE BEST AVAILABLE COPY.

As rescanning these documents will not correct the image problems checked, please do not report these problems to the IFW Image Problem Mailbox.